



UPPSALA UNIVERSITET

First principles calculations of 2D materials

Author

Jacob WESTHOLM

Supervisor

Biplab SANYAL

Co-supervisor

Raquel ESTEBAN PUYUELO

Subject reader

Oscar GRÅNÄS

Uppsala University, Department of Physics and Astronomy

June 25, 2018

BACHELOR THESIS IN PHYSICS, 15 HP

Abstract

In this project, Density Functional Theory as implemented in Quantum Espresso is used to calculate the electronic structures of monolayers and bulk of MoS₂ and WTe₂. The calculations are carried out for four different types of pseudopotentials generated using PSlibrary. It is found that the band structure of monolayer MoS₂ is only properly described for the pseudopotentials including spin-orbit coupling. In addition to this, a simple test was preformed to check the transferability of the pseudopotentials by calculating the bulk modulus and lattice constants of molybdenum, tungsten and tellurium. The results obtained with the generated pseudopotentials were found to be in line with expectations. indicating that the pseudopotentials have a good transferability.

Sammanfattning

I denna studie används tätthetsfunktionalteori implementerad i Quantum Espresso för att beräkna elektronstrukturer för MoS₂ och WTe₂" i bulk och två dimensionell form.. Beräkningarna har utförts för fyra olika pseudopotentialer hämtade från PSlibrary. Det visar sig att bandstrukturen för två dimensionell MoS₂ enbart beskrivs korrekt för pseudopotentialer som inkluderar effekten av spinn bankkoppling. Dessutom utfördes ett test av överförbarheten för pseudopotentialerna genom att beräkna trykmodul och gitterkonstanter för bulk molybden, bulk volfram och trigonal tellur. Framräknade värden för pseudopotentialerna var i enhetlighet med experimentelavärden, vilket indikerar att pseudopotentialerna har en god överförbarhet.

Contents

| | |
|---------------------------------------------------------------------------|----|
| Part I: Background | 5 |
| 1 Introduction | 7 |
| 2 Theoretical background | 9 |
| 2.1 Basic Solid State Physics | 9 |
| 2.1.1 Crystal lattices | 9 |
| 2.1.2 Reciprocal lattice | 11 |
| 2.1.3 Bloch's theorem | 11 |
| 2.1.4 Band structure | 12 |
| 2.1.5 The Fermi energy | 13 |
| 2.2 Density functional theory | 17 |
| 2.2.1 The correlated electron many-body problem | 17 |
| 2.2.2 Introduction to Density Functional Theory | 18 |
| 2.2.3 The Hohenberg-Kohn theorems and the Kohn-Sham equations | 19 |
| 2.2.4 Plane waves and Pseudopotentials | 24 |
| Part II: Method ,Results and Discussion | 27 |
| 3 Project | 29 |
| 3.1 Computational Details | 29 |
| 3.2 Quantum Espresso and Pslibrary | 31 |
| 3.3 Test systems | 31 |
| 3.3.1 Si | 31 |
| 3.3.2 Graphene | 34 |
| 3.3.3 Hexagonal Boron Nitride | 35 |
| 3.4 TMDs | 36 |
| 3.4.1 Tungsten ditelluride (WTe ₂) | 36 |
| 3.4.2 MoS ₂ | 41 |
| 3.5 Transferability of Pseudopotentials | 52 |
| 3.5.1 Mo | 52 |
| 3.5.2 W | 53 |
| 3.5.3 Te | 56 |
| 4 Conclusion and outlook | 58 |
| 5 Acknowledgments | 59 |
| References | 60 |

Part I:

Background

1. Introduction

The development of transistors used in the electronics industry has during the last decades been driven by the continued development of smaller and smaller transistors. However the continued decrease of transistors size will soon be approaching its limits due to quantum mechanical effects. In order to continue the development, there is a need of developing new materials with suitable electronic properties that can replace the silicon based electronics used today.

Since the experimental realization of graphene a single layer of graphite in 2004, two dimensional materials are at the focus of solid state research [1, 2]. Graphene with its remarkable characteristics has been proposed for diverse applications, especially as a replacement for silicon in the electronics industry [3]. Graphene is however not suitable for application in field-effect transistors (used in logical applications), due to its lack of a band gap [3, 4, 5]. This has led to a search for other two-dimensional materials with a suitable band gap and similar properties.

One of the material types that has received attention is monolayers of transition metal dichalcogenides (TMDs). The TMDs are materials of the form MX_2 where M is a transition metal e.g. Mo, W, V, Nb and X is a chalcogen e.g. S, Se, Te [5]. Among the 2 dimensional TMDs, some show semiconducting behaviour with a band gap in the visible spectrum e.g. MoS_2 , making them suitable for field-effect transistors and optoelectronics. [5, 6]

In order to find and study materials with suitable electrical properties a wide range of theoretical and experimental methods is used. The most commonly used method for theoretical calculations is density functional theory (DFT), a method where the electronic structure is described as a functional of the electronic density. There are a number of different numerical implementations of DFT using different approximations. In this project, DFT using planewaves and pseudopotential approximations is used. This project has been carried out using the Quantum Espresso software with pseudopotentials from PSlibrary¹. In this project band structures of two types of TMDs are calculated for different stacking using different pseudopotentials. The band structures obtained are then compared to experimental results to see if the pseudopotentials manage to accurately describe the characteristics of the real band structures.

In the first part of this report, a background to the theory used in this thesis is described. giving a more detailed explanation of density functional theory

¹ PSlibrary is a library of pseudopotentials that can be used together with ld1.x code of Quantum Espresso. Some of these pseudopotentials are already available to be downloaded from the Quantum Espresso homepage.

and pseudopotentials. Secondly, the methods used for the calculations are explained and exemplified for some sample systems. Lastly, the result from the band structure calculations on two TMDs together with some simple tests of the transferability of the pseudopotentials are presented and discussed.

2. Theoretical background

2.1 Basic Solid State Physics

2.1.1 Crystal lattices

In the description of ordered materials, it is of great use to extend the system into an infinite crystal. The infinite ordered crystal may be described using the formalism of a Bravais lattice with a basis. The Bravais lattice is an array of infinite points with the same neighborhoods or more precisely it may be defined by two equivalent definitions as given by Ashcroft and Mermin[7, p. 64-65]:

- (a) A Bravais lattice is an infinite array of discrete points with an arrangement and orientation that appears exactly the same from whichever of the points the array is viewed
- (b) A (three-dimensional) Bravais lattice consists of all points with position vectors \mathbf{R} of the form

$$\mathbf{R} = n_1 \mathbf{a}_1 + n_2 \mathbf{a}_2 + n_3 \mathbf{a}_3, \quad (2.1)$$

where \mathbf{a}_1 , \mathbf{a}_2 and \mathbf{a}_3 are any three vectors not all in the same plane and n_1 , n_2 and n_3 range through all integer values. Thus the point $\sum n_i \mathbf{a}_i$ is reached by moving n_i steps of length a_i in the direction of \mathbf{a}_i for $i=1,2$ and 3.

The vectors \mathbf{a}_i appearing in definition of Bravais lattice are called primitive vectors and are said to generate or span the lattice.[7, p. 64-65]

To apply the concept of Bravais lattices to crystal one needs also to specify a crystal basis describing which elements are present and where these elements are placed in relation to the Bravais lattice points. e.g. the position of the two carbon atoms per Bravais lattice point in graphene needs to be written in the form of:

$$\{C_j\} = \sum_i n_i \mathbf{a}_i + \mathbf{b}_j, \forall n_i \in \mathbb{Z}, \quad j \in \{1, 2\} \quad (2.2)$$

Another important concept of the crystal lattice is the unit cell. There are two types of unit cells that are used: primitive unit cells and conventional unit cells. A primitive unit cell is a cell of space around a lattice point that when translated through all the Bravais lattice vectors fills all space of the crystal without overlapping. The conventional unit cell is a unit cell that fills all of space when translated through only a subset of the Bravais lattices. Among all the possible choices of primitive unit cells the most important and commonly

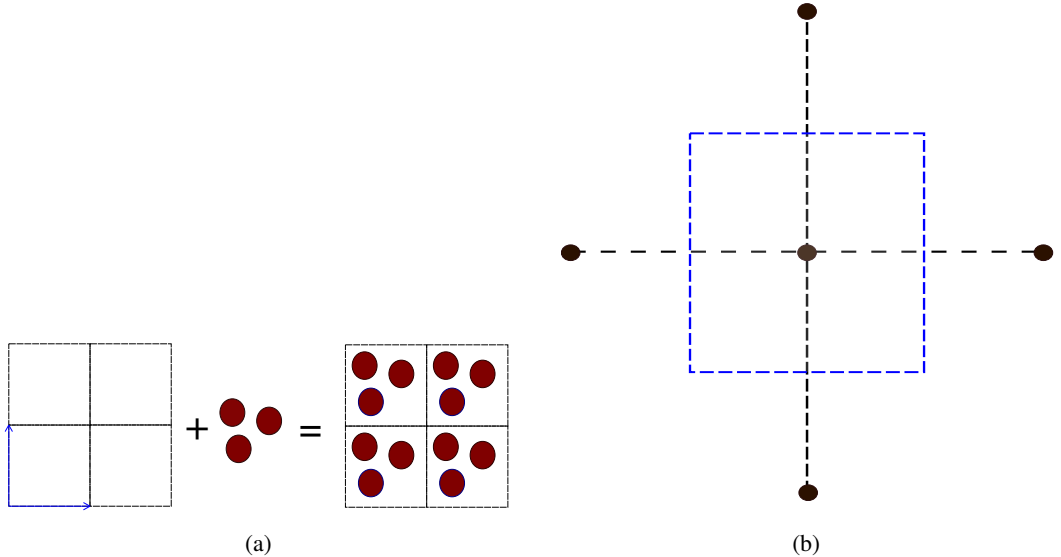


Figure 2.1. (a) shows a two dimensional lattice with a basis. (b) shows an example of a Wigner-Seitz unit cell in blue, The dashed black lines indicates the straight path in between lattice points.

used is the Wigner-Seitz cell. The Wigner-Seitz cell for a Bravais lattice point consists of all the points that are closer to the lattice point than any other Bravais lattice point [7]. The general concept of a lattice with basis and the Wigner-Seitz unit cell is shown in figure 2.1.

The unit cells are often characterized by the six lattice parameters a, b, c, α, β and γ where a, b, c are lengths of the sides of the unit cell and α, β and γ are angles in the unit cell. These parameters are defined as in figure 2.2.

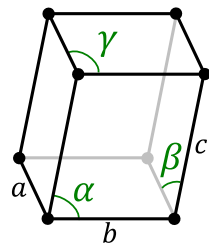


Figure 2.2. Sketch of a unit cell showing how the lattice parameters are defined. figure taken from [8]

2.1.2 Reciprocal lattice

Crystals are well suited for treatment in the reciprocal space due to their periodic nature. When considering plane waves having the periodicity of the Bravais lattice a set of reciprocal vectors that makes up a Bravais lattice in reciprocal space arises naturally. These reciprocal lattice points can be written in the same form as in equation 2.1 [7]i.e.:

$$\mathbf{K} = k_1 \mathbf{b}_1 + k_2 \mathbf{b}_2 + k_3 \mathbf{b}_3, \quad \forall k_1, k_2, k_3 \in \mathbb{Z} \quad (2.3)$$

where \mathbf{K} denotes the reciprocal lattice points and $\mathbf{b}_1, \mathbf{b}_2$ and \mathbf{b}_3 are reciprocal primitive vectors given by:

$$\mathbf{b}_1 = 2\pi \frac{\mathbf{a}_2 \times \mathbf{a}_3}{\mathbf{a}_1 \cdot (\mathbf{a}_2 \times \mathbf{a}_3)} \quad (2.4)$$

$$\mathbf{b}_2 = 2\pi \frac{\mathbf{a}_3 \times \mathbf{a}_1}{\mathbf{a}_1 \cdot (\mathbf{a}_2 \times \mathbf{a}_3)} \quad (2.5)$$

$$\mathbf{b}_3 = 2\pi \frac{\mathbf{a}_1 \times \mathbf{a}_2}{\mathbf{a}_1 \cdot (\mathbf{a}_2 \times \mathbf{a}_3)} \quad (2.6)$$

These equations arise from the condition that \mathbf{K} should fulfill the condition:

$$e^{i \mathbf{K} \cdot \mathbf{R}} = 1 \quad (2.7)$$

Since the reciprocal lattice is also a Bravais lattice it is also possible to define the Wigner-Seitz primitive cell of the Bravais lattice which is called the first Brillouin Zone.

2.1.3 Bloch's theorem

For the system of non interacting electrons (i.e. the electron-electron interaction have been put in an effective external potential) in a periodic potential $U(\mathbf{r})$ one can derive a general form for the wavefunction of the electron. This result is called Bloch's Theorem and is formulated as follows by Ashcroft and Mermin[7, p. 133-134]:

Theorem The eigenstates ψ of the one electron Hamiltonian: $-\frac{\hbar^2}{2m} \nabla^2 + U(\mathbf{r})$, where $U(\mathbf{r} + \mathbf{R}) = U(\mathbf{r})$ for all \mathbf{R} in a Bravais lattice, can be chosen to have the form of a plane wave times a function with the periodicity of the Bravais lattice:

$$\psi_{n\mathbf{k}}(\mathbf{r}) = e^{i\mathbf{k} \cdot \mathbf{r}} u_{n\mathbf{k}}(\mathbf{r}) \quad (2.8)$$

where

$$u_{n\mathbf{k}}(\mathbf{r} + \mathbf{R}) = u_{n\mathbf{k}}(\mathbf{r}) \quad (2.9)$$

for all \mathbf{R} in the Bravais lattice. [...] Bloch's theorem is sometimes stated in the in this alternative form: the Eigenstates of H can be chosen so that associated with each ψ is a wave vector \mathbf{k} such that:

$$\psi(\mathbf{r} + \mathbf{R}) = e^{i\mathbf{k}\cdot\mathbf{R}}\psi(\mathbf{r}) \quad (2.10)$$

for every \mathbf{R} in the Bravais lattice[7, p. 133-134].

The proof of Bloch's theorem relies simply on the periodicity of the Hamiltonian, however it does not state anything about the allowed values of the wave vector \mathbf{k} . By imposing the so called Born-von Karman boundary condition it can be shown that the allowed space for each of the \mathbf{k} vectors are given by.

$$V_k = \frac{(2\pi)^3}{N} \quad (2.11)$$

Where V_k is the volume per \mathbf{k} point, N is the total number of primitive cells. Since the number of primitive cells in a crystal is large this means that the allowed wave vectors will behave as a continuum. even though this means that the allowed values for the \mathbf{k} vector is defined over the entire crystal the points of interest can be confined inside the first Brillouin zone by noting that for \mathbf{k} outside of the first Brillouin zone \mathbf{k} can be written as $\mathbf{k} = \mathbf{k}' + \mathbf{K}$ where \mathbf{K} is a vector in the reciprocal lattice and \mathbf{k}' is inside the Brillouin zone.

2.1.4 Band structure

Since the wavefunctions are dependent on the wave vector so must the energies of the electrons be, which means the following relation for the energies can be written:

$$\epsilon_{n,\mathbf{k}+\mathbf{K}} = \epsilon_{n,\mathbf{k}}, \quad (2.12)$$

where the energies dependent on the \mathbf{k} vectors are known as the band structure. In general the \mathbf{k} vector is a 3-dimensional vector so to be able to visualize the information, the band structure is plotted along lines of interest in the first Brillouin zone.[7]

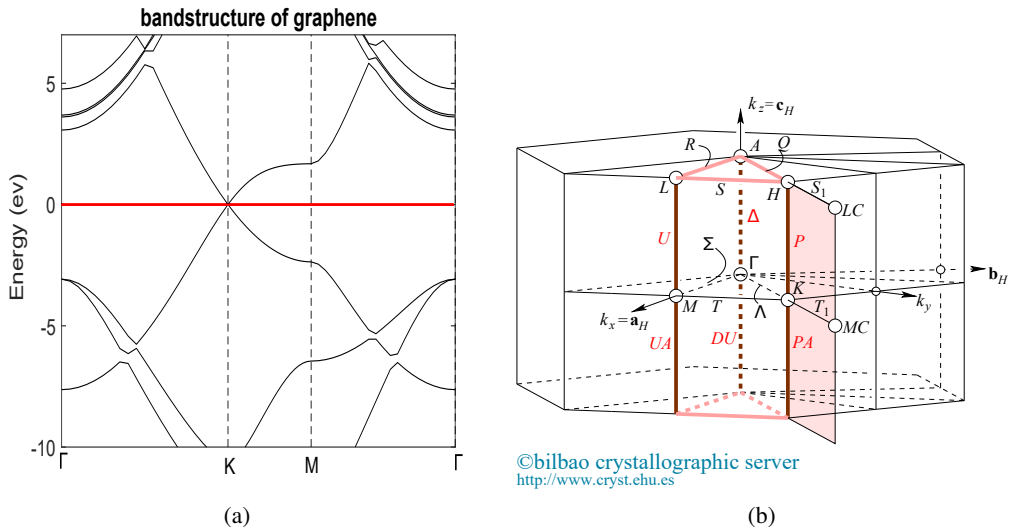


Figure 2.3. (a) Band structure of graphene from data created with Quantum Espresso plotted along high symmetry lines. The Fermi energy is shown as a horizontal straight line and is taken to be zero. (b) A sketch showing the Brillouin zone of graphene. The band structure is calculated along path between the points $\Gamma - K - M - \Gamma$ where the points are marked in the figure. The figure was taken from [9].

2.1.5 The Fermi energy

For a system of N electrons, only a part of the band structure will be occupied. Since the electrons obey the Pauli exclusion principle, two electrons can't occupy the same state, this means that the bands will be filled by electrons from the lowest energy and upwards. The energy in between the highest occupied energy level and the lowest unoccupied energy level is known as the Fermi energy. Dependent on the system there are two principal ways the bands may be filled:

1. There may be bands that are partially filled so that the Fermi energy will intersect one or more bands
2. All occupied bands may be filled with an energy gap in between the highest occupied and lowest unoccupied bands.

Dependent on how the bands are filled the material will have different electronic properties. If the electrons are distributed as in case 1 they will have metallic properties and if they are distributed as in case 2 they will behave like a semiconductor or an insulator dependent on if the energy gap¹ is large in comparison with $K_B T$ at room temperature. Where K_B is the Boltzmann constant and T is the temperature.

¹The energy difference between the highest occupied and lowest unoccupied bands

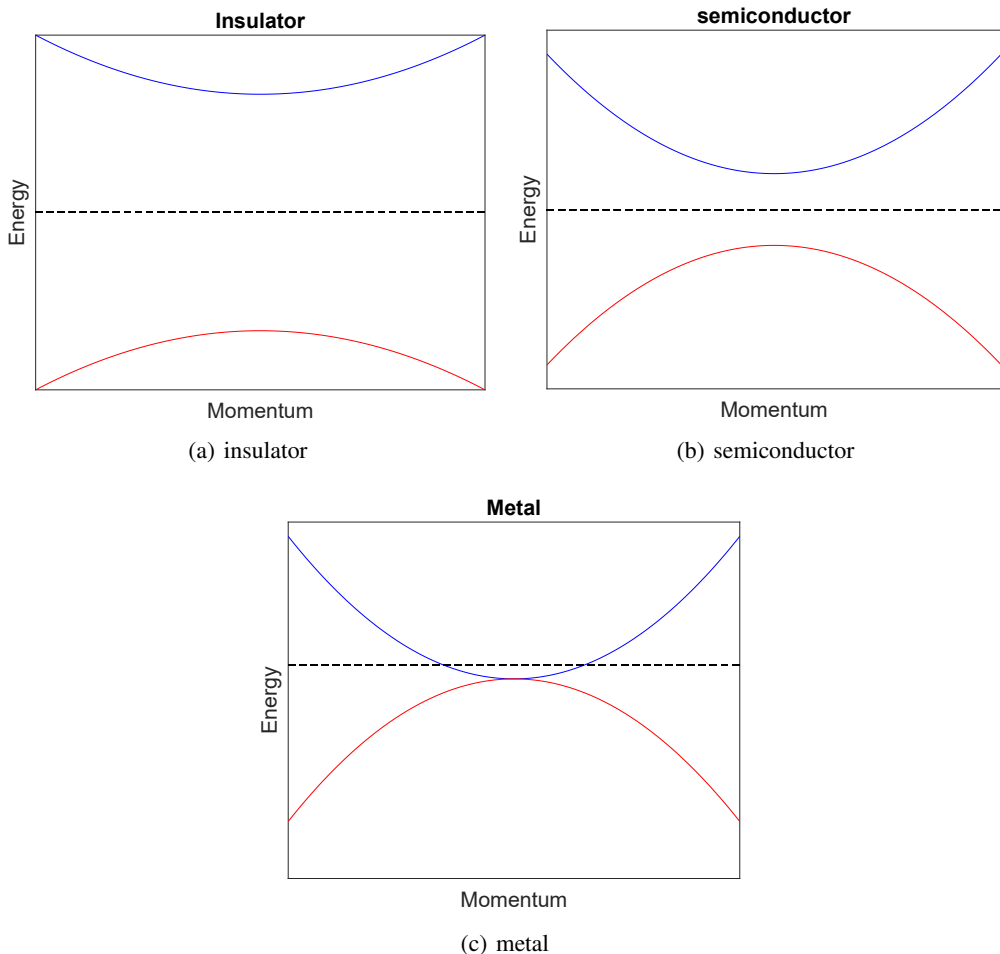


Figure 2.4. Sketches of the highest occupied and lowest unoccupied band, showing the different cases of electronic properties. The bands are sketch as blue and red parabolas and the Fermi energy is sketch as a black line

Spin-orbit coupling

The effect of spin-orbit coupling is important for the band structure of crystals, since the spin-orbit coupling lifts the degeneracy for some of the bands. The spin orbit coupling is an effect that arises inside the atom and is given by the coupling of the electron's spin angular momentum with the orbital angular momentum. A derivation of the spin-orbit effect can be found in textbooks on quantum mechanics such as [10] and the effect is given by the following Hamiltonian:

$$\hat{H}_{SO} = -\frac{1}{2m^2c^2} \frac{1}{r} \frac{dV(r)}{dr} \hat{S} \cdot \hat{L} \quad (2.13)$$

where \hat{S} is the spin angular momentum operator, \hat{L} is the orbital angular momentum operator and $V(r)$ is the potential of the atom. In the treatment of spin orbit coupling in atoms, the effect can often be treated as a perturbation and the effects calculated for an atom can often be carried over to crystals since the effect originates close to the core. The effects on crystals are dependent on the symmetry of the crystal structure and the spin-orbit interaction only splits the bands of crystal structures that break the space inversion symmetry. [11, 7].

Density of states

Density of states is another quantity of importance, and can be thought of as the number of energy states per energy and volume. The density of states is given by [7, 12]:

$$g(\varepsilon) = \sum_n g_n(\varepsilon) \quad (2.14)$$

$$g_n(\varepsilon) = \int \frac{d\mathbf{k}}{4\pi^3} \delta(\varepsilon - \varepsilon_n(\mathbf{k})) \quad (2.15)$$

Where $g_n(\varepsilon)$ s are the density of states of the n:th band and the integral in the second equation is taken over the first Brillouin zone with δ denoting the Dirac delta-function involving the eigenvalue $\varepsilon_n(\mathbf{k})$ for the n:th band at the reciprocal point \mathbf{k} .

The density of states of Graphene are plotted together with the band structure in figure 2.5.

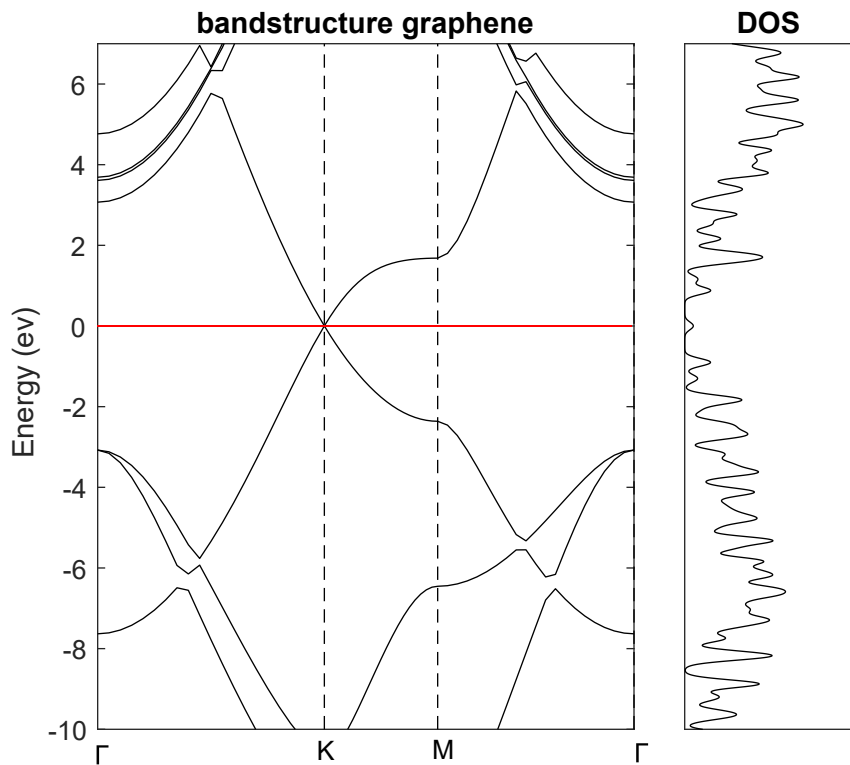


Figure 2.5. The bandstructure of graphene together with the DOS show to the right. The picture was plotted from data created using Quantum Espresso and the Fermi energy has been taken to be zero.

2.2 Density functional theory

2.2.1 The correlated electron many-body problem

The fundamental problem of describing materials is that of describing the system of interacting electrons and nuclei. The electronic properties of such a system containing N electrons can be obtained by solving the many-body Schrödinger equation:

$$H\Psi(\mathbf{r}_1, \mathbf{r}_2, \dots, \mathbf{r}_n, \mathbf{R}_1, \mathbf{R}_2 \dots) = E\Psi(\mathbf{r}_1, \mathbf{r}_2, \dots, \mathbf{r}_n, \mathbf{R}_1, \mathbf{R}_2 \dots) \quad (2.16)$$

Where the \mathbf{r}_i is the position vectors for the electron and the \mathbf{R}_I is the position vectors of the ions. The Hamiltonian of such a system is:

$$\begin{aligned} \hat{H} = & -\frac{\hbar^2}{2m_e} \sum_i \nabla_i^2 - \sum_{i,I} \frac{e^2 Z_I}{|\mathbf{r}_i - \mathbf{R}_I|} + \frac{1}{2} \sum_{i \neq j} \frac{e^2}{|\mathbf{r}_i - \mathbf{r}_j|} \\ & - \sum_I \frac{\hbar^2}{2M_I} \nabla_I^2 + \frac{1}{2} \sum_{I \neq J} \frac{e^2 Z_I Z_J}{|\mathbf{R}_I - \mathbf{R}_J|} \end{aligned} \quad (2.17)$$

where m_e is the electron mass, M_I is the mass of the I:th ion, \hbar is the Planck constant divided by 2π , e is the electron charge, Z_I is the atomic number of the I:th ion, \mathbf{r}_i is the position vector of i:th electron, \mathbf{R}_I is the position vector of the I:th Ion and ∇_i^2 , ∇_I^2 are the laplacian operators with respect to \mathbf{r}_i and \mathbf{R}_I respectively. In equation 2.17 sums over the lower case indices run over all electrons and the sums over the upper case indices run over all ions.

By use of the Born-Oppenheimer approximation (i.e. realizing that the electrons with much lighter mas move much faster than the ions so that the motion of the two degrees of freedom can be decoupled and hence the kinetic energy of the ions can be neglected.) the problem may be reduced to:

$$\hat{H} = -\frac{\hbar^2}{2m_e} \sum_i \nabla_i^2 - \sum_{i,I} \frac{e^2 Z_I}{|\mathbf{r}_i - \mathbf{R}_I|} + \frac{1}{2} \sum_{i \neq j} \frac{e^2}{|\mathbf{r}_i - \mathbf{r}_j|} + \frac{1}{2} \sum_{I \neq J} \frac{e^2 Z_I Z_J}{|\mathbf{R}_I - \mathbf{R}_J|} \quad (2.18)$$

This problem will be referred to as the correlated electron many-body problem or the electron many-body problem or simply the many-body problem through out the rest of this report.

It is usual to denote the different parts of the Hamiltonian by

$$\hat{H} = \hat{T} + \hat{V}_{ext} + \hat{V}_{int} + E_{II} \quad (2.19)$$

where

$$\hat{T} = -\frac{\hbar^2}{2m_e} \sum_i \nabla_i^2 \quad (2.20)$$

$$\hat{V}_{ext} = -\sum_{i,I} \frac{e^2 Z_I}{|\mathbf{r}_i - \mathbf{R}_I|} \quad (2.21)$$

$$\hat{V}_{int} = \frac{1}{2} \sum_{i \neq j} \frac{e^2}{|\mathbf{r}_i - \mathbf{r}_j|} \quad (2.22)$$

$$E_{II} = +\frac{1}{2} \sum_{I \neq J} \frac{e^2 Z_I Z_J}{|\mathbf{R}_I - \mathbf{R}_J|} \quad (2.23)$$

\hat{T} is the kinetic energy operator of the system, V_{ext} denotes the external potentials from the ions, V_{int} is the internal potential between the electrons and E_{II} describes the ion ion interaction.

Equation 2.19 is a non relativistic equation, however relativistic effects such as spin-orbit coupling² can often be included using perturbation theory. The inclusion of spin-orbit coupling is of importance since it may lift degeneracies in the band structure. [12]

Even if Born-Oppenheimer approximation simplifies the many-body Schrödinger equation it is still impossible to solve the problem exactly for anything more complicated than a single atom. The preferred method is then to solve it numerically however the Hamiltonian in equation 2.18 is not well suited for solving numerically, since the number of variable scales like 3 times the number of electrons and there can be on the order of 10^{23} electrons in a solid. Density functional Theory was introduced in order to reduce the number of variables and make the problem better suited for numerical techniques Density functional Theory achieves this by substituting the many-body wavefunction with the electron density [13].

2.2.2 Introduction to Density Functional Theory

Density functional theory (DFT) is a first principles method for calculating the electron structure of real materials. DFT dates back to an article 1964 by P. Hohenberg and W. Kohn [14] where they showed that the total energy of a system can be expressed as a functional of the electron density $n(r)$, $E = E[n(r)]$ where the exact form of $E[n(r)]$ is not known. Later, Kohn and Sham constructed a Schrödinger like equation to solve a single electron problem in a mean field manner. In implementations of DFT, different approximations are used in order to calculate the electron structure [15]. From the electron structure different ground state properties of materials can be calculated e.g.

²spin orbit coupling is the coupling between the spin and the angular momenta in the atom

structural, magnetic, optical, mechanical etc [16]. In the last decade, the uses of DFT in materials science has increased many fold and is now one of the preferred methods for examining materials.[14]

In the rest of this chapter the equations will be written using Hartree atomic units if nothing else is stated. Hartree atomic units are defined as:

$$\hbar = m_e = e = 4\pi/\epsilon_0 = 1$$

2.2.3 The Hohenberg-Kohn theorems and the Kohn-Sham equations

The Hohenberg-Kohn theorems

The foundation of DFT lies in the statement of the Hohenberg-Kohn theorems, which show that the electron many-body system may be fully determined by the ground state electron density ($n_0(r)$). Allowing at least in principle the replacement of a problem dependent on the n vectors of the n electron wavefunction $\Psi(\mathbf{r}_1, \mathbf{r}_2, \dots, \mathbf{r}_n)$ with a problem dependent s on a scalar function $n(r)$. This replacement is of great importance as the number of atoms in a system is increased and is one of the reasons for the success of DFT [13].

The theorems can be stated as given by Martin[12, p.122] for a non degenerate system:

Theorem I: For any system of particles in an external potential $V_{ext}(\mathbf{r})$, the potential $V_{ext}(\mathbf{r})$ is determined uniquely, except for a constant, by the ground state particle density $n_o(\mathbf{r})$ [12, p.122].

Theorem II: A universal functional for the energy $E[n]$ in terms of the density $n(\mathbf{r})$ can be defined by valid for any external potential $V_{ext}(\mathbf{r})$ for any particular $V_{ext}(\mathbf{r})$, the exact ground state energy of the energy is the global minimum value of this functional, and the density $n(\mathbf{r})$ that minimizes the functional is the exact ground state density $n_0(\mathbf{r})$ [12, p.122].

The first theorem means that in principle the whole system is determined by the ground state density, since the potential V_{ext} determines the Hamiltonian, which in its turn leads to the wavefunction. The functional described in Theorem II is the total energy functional defined as:

$$E[n] \equiv F_{HK}[n] + \int d^3r V_{ext}(\mathbf{r}) n(\mathbf{r}) + E_{II}, \quad (2.24)$$

where E_{II} describes the ion-ion interaction. The F_{HK} functional is defined from the electron many-body problem as:

$$F_{HK}[n] = \langle \hat{T} \rangle + \langle \hat{V}_{int} \rangle \quad (2.25)$$

where \hat{T} and \hat{V}_{int} is given by equation 2.20 , 2.22 [13, 12].

Kohn-Sham equations

Even though the Hohenberg-Kohn theorems define a functional of the total energy that is in principle only dependent on the electron density the F_{HK} functional is not known in a way that does not explicitly contain the electron many-body wavefunction. Instead of using the total energy functional directly Kohn and Sham suggested a method for replacing the full many-body problem with an independent particle problem having the same ground state density[13, 12].

The use and construction of the non interacting system is dependent on two assumptions: the existence of a non-interacting system that has the same ground state as the ground state of the many-body problem of interest and secondly that the Hamiltonian of the non-interacting system (NI-system) has the usual independent particle momentum operator and that the electrons experience an effective potential V_{eff} .

$$\hat{H}_{eff} = -\frac{1}{2}\nabla^2 + V_{eff}(\mathbf{r}) \quad (2.26)$$

From these assumptions, an energy functional can be created for the NI-system, which for doubly-occupied electronic wavefunctions ψ_i it can be written as [16]:

$$E[\{\psi_i\}] = -\sum_i \int \psi_i \nabla^2 \psi_i d^3\mathbf{r} + \int V_{ext}(\mathbf{r}) n(\mathbf{r}) d^3\mathbf{r} \\ + \frac{1}{2} \int \frac{n(\mathbf{r})n(\mathbf{r}')}{|\mathbf{r} - \mathbf{r}'|} d^3\mathbf{r} d^3\mathbf{r}' + E_{xc}[n(\mathbf{r})] + E_{II}(\{R_I\}) \quad (2.27)$$

ψ_i are the wavefunctions of the NI-system, \mathbf{r} is the position vector of the electron, V_{ext} is external potential from the ions, E_{II} is the ion ion energy functional defined in equation 2.23 and E_{xc} is the exchange correlation functional describing the effect of Coulomb exchange and correlation and the Pauli exclusion principle from the original many-body problem. \mathbf{R}_I s are the position vectors of the ions and $n(\mathbf{r})$ is the electron density which for a doubly occupied NI-system may be written as:

$$n(\mathbf{r}) = 2 \sum_i |\psi_i|^2 \quad (2.28)$$

Collecting the terms in equation 2.27:

$$E = T_s[n] + \int V_{ext}(\mathbf{r}) n(\mathbf{r}) d^3\mathbf{r} + E_{Hartree}[n] + E_{xc}[n] + E_{II}, \quad (2.29)$$

where T_s is the kinetic energy of the NI-system and $E_{Hartree}$ is the electron-electron interaction without the exchange and correlation effects defined by:

$$T_s[n] = - \sum_i \int \psi_i \nabla^2 \psi_i d^3 \mathbf{r} \quad (2.30)$$

$$E_{Hartree}[n] = \frac{1}{2} \int \frac{n(\mathbf{r})n(\mathbf{r}')}{|\mathbf{r} - \mathbf{r}'|} d^3 \mathbf{r} d^3 \mathbf{r}' \quad (2.31)$$

In the Kohn-Sham equations the effects of exchange and correlation of the original many-body wavefunction have been put in the exchange-correlation functional. If this functional had been known, the minimization of equation 2.29 would have yielded the exact ground state energy and density of the many-body problem via the Schrödinger-like Kohn-Sham equations.

$$\left[-\frac{1}{2} \nabla^2 + V_{ext}(\mathbf{r}) + V_{Hartree} + V_{xc} \right] \psi_i(\mathbf{r}) = \epsilon_i \psi_i(\mathbf{r}) \quad (2.32)$$

where $V_{Hartree}$ and V_{xc} is defined by

$$V_{Hartree} = \frac{\delta E_{Hartree}}{\delta n(\mathbf{r})} \quad (2.33)$$

$$V_{xc} = \frac{\delta E_{xc}}{\delta n(\mathbf{r})} \quad (2.34)$$

Equation 2.32 and 2.29 allow for the formulation and implementation of self-consistent field methods using approximate exchange correlation functionals. The self consistent field methods(SCF) follows the flow scheme that can be seen in figure 2.6.

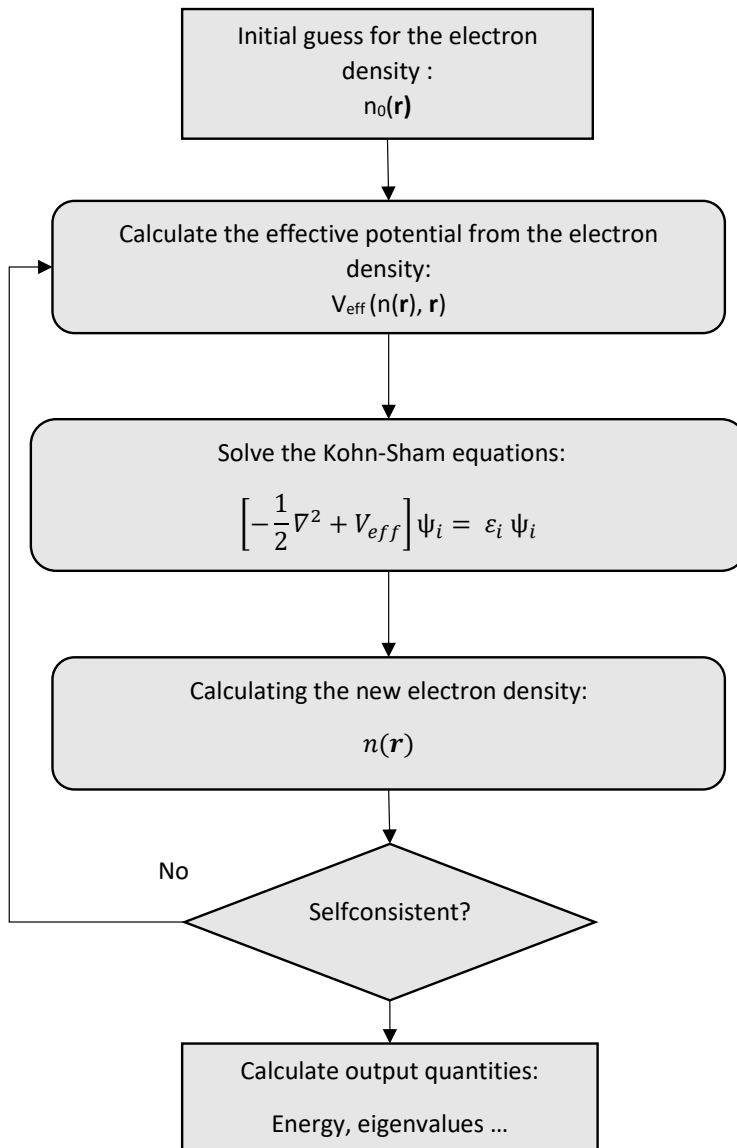


Figure 2.6. Flowchart that describes an SCF implementation of DFT.

The Exchange Correlation functional

The Kohn-Sham equation is a mapping of the many-body problem onto a system of non-interacting electrons. To properly map the many-body system onto a NI-system effects such as the Pauli exclusion principle and the restriction on motion due to the presence of the other electrons must be taken into account. These effects are called exchange and correlation. In DFT, the effects of correlation and exchange in the original many-body problem are replaced by the exchange correlation functional $E_{xc}[n]$. There are however no known analytic forms for the exchange correlation functional. This has led to the development of approximations for the exchange correlation functional.

The first proposed approximation for DFT was the local density approximation (LDA) [17]. In LDA, the exchange correlation energy is approximated by the exchange correlation energy of a "homogeneous" electron gas, where the density of the electron gas is taken to be the same as the local electron density:

$$E_{xc}^{LDA} = \int d^3\mathbf{r} n(\mathbf{r}) \epsilon_{xc}(n(\mathbf{r})) \quad (2.35)$$

ϵ_{xc} is the exchange-correlation energy density of a homogeneous electron gas with a uniform positive background charge so that the system is electrically neutral. The exchange correlation energy can be divided into an exchange part and a correlation part:

$$\epsilon_{xc}(n(\mathbf{r})) = \epsilon_c(n(\mathbf{r})) + \epsilon_x(n(\mathbf{r})) \quad (2.36)$$

For the simple case of the homogeneous electron gas there is an analytic expression for the exchange energy (ϵ_x). However there is no analytic formula for the correlation energy (ϵ_c), instead the value of the correlation energies has been calculated numerically using quantum Monte Carlo methods making it possible to create accurate, exchange correlation energies $\epsilon_{xc}(n)$.

Since the introduction of DFT, there has been many attempts to improve upon the LDA among these are a group of exchange correlation functionals called generalized gradients approximation(GGA) where the GGA takes into account the gradient of the electron density:

$$E_{xc}^{GGA} = \int d^3\mathbf{r} n(\mathbf{r}) \epsilon_{xc}(n(\mathbf{r}), \nabla n(\mathbf{r})) \quad (2.37)$$

here ϵ_{xc} is the exchange correlation energy and the form it takes depends on which GGA method is chosen.

The way of constructing a functional of the GGA form is not trivial and different functionals managed to satisfy different conditions on the exchange energies while breaking others. However in the region of density that is relevant to most physics the difference between the methods is small [12, 18].

2.2.4 Plane waves and Pseudopotentials

Plane waves basis

In order to solve the Kohn-Sham equations (equation 2.32) a basis for treating the problem needs to be chosen. Due to Bloch's theorem it is natural to use planewaves since the NI-system may be easily represented using plane waves. The terms in the Hamiltonian can be expanded in terms of their Fourier series and the wavefunction in terms of plane waves using Bloch's theorem. Equation 2.32 can then be expressed as:

$$\sum_{G'} \left(\frac{1}{2} |\mathbf{k} + \mathbf{G}|^2 \delta_{\mathbf{G}, \mathbf{G}'} + V_{ext}(\mathbf{G} - \mathbf{G}') + V_{Hartree}(\mathbf{G} - \mathbf{G}') + V_{xc}(\mathbf{G} - \mathbf{G}') \right) c_{i, \mathbf{k} + \mathbf{G}'} = \varepsilon_i c_{i, \mathbf{k} + \mathbf{G}} \quad (2.38)$$

Here the $c_{i, \mathbf{k} + \mathbf{G}}$ s are the coefficients of the plane waves used for the expansion wave function. The potentials are the Fourier components of the Fourier representation of the potentials. ε :S denote the eigenenergies in Kohn-Sham equation and the G's denote reciprocal lattice vectors.

The sum in equation 2.38 is infinite however one may truncate the problem by choosing a maximum energy cutoff. This leads to a finite basis set of plane waves that can be used in approximate methods of solving the Kohn-Sham equations. The computational cost of solving the system in using plane waves is primarily dependent on the number of electrons considered and how large the cutoff energy is taken to be. In order to reduce the computational burden of plane wave based DFT, one may use so called pseudopotentials.[16]

Introduction to pseudopotentials

The use of plane waves to describe the valence electron wavefunctions (v.e. wavefunction) is a natural one since the valence electrons behave almost like free particles away from the core. However around the core the v.e. wavefunctions oscillate rapidly due to the tightly bound core electrons. This means that to accurately describe the v.e. wavefunctions, a large number of plane waves is needed. Since the use of many plane waves is computationally expensive it is not feasible to use plane waves to solve the Kohn-Sham equations without introducing other approximations.

The general idea behind the usage of pseudopotentials is to replace the effect of the tightly bound core electrons and the strong Coulomb potential with a weaker effective potential, allowing for the construction of smoother pseudo wavefunctions. The pseudopotential and pseudo wavefunctions are constructed so that they are equal to the real potential and wavefunction outside the core region defined by the core radius r_c and that the phase shift of the pseudo system equals that of the original system like in figure 2.7. The exclusion of the core electrons from the calculations means that the information of what happens in the core is lost, however most of the physical properties depend primarily on the valence electrons allowing for the removal of

the core electrons while keeping a high accuracy in the prediction of physical properties.[16, 12, 7]

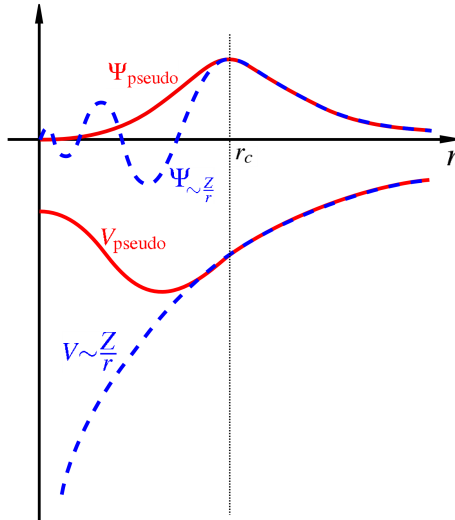


Figure 2.7. A sketch of a pseudopotential and the corresponding pseudo wavefunction (red solid lines) together with a sketch of the original Coulomb potential and valence electron wavefunction (blue dotted line). Where the ion is placed at $r=0$ and the dotted black line indicates the end of the core region and the beginning of the bonding region. The pseudopotential and pseudowavefunctions are equal to the true wavefunction and potential outside the core region.(The images was taken from [19])

Ultrasoft pseudopotentials and Projector augmented-wavefunctions

Projector augmented-wave method

The Projector augmented-wavefunction (PAW) is based on the Orthogonal plane waves (OPW) method but is more suitable to total energy calculations. The general idea of The PAW is to express the v.e.wavefunction by pseudo wavefunctions and a linear Transformation using so called projector functions :

$$|\Psi\rangle = T |\Phi\rangle, \quad (2.39)$$

where T is the linear transformation Ψ is v.e.wavefunction and Φ is the pseudo v.e. wavefunction. Around each core the pseudo and v.e. wavefunction may be expanded using partial waves functions:

$$|\Phi\rangle = c_n |\phi_n\rangle \quad (2.40)$$

$$|\Psi\rangle = c_n |\psi_n\rangle \quad (2.41)$$

Equation 2.40 ,2.41 and 2.39 imply the existence of projector functions (P_n) around each core full filling:

$$\langle P_a | \phi_n \rangle = \delta_{a,n} \quad (2.42)$$

where P_a is the projector function and $\delta_{a,n}$ is the Kronecker delta function. This gives the following form for the linear transformation:

$$T = 1 + \sum_n (|\psi_n\rangle - |\phi_n\rangle) \langle P_n | \quad (2.43)$$

One of the advantages of the method is that operators may be transformed to operators only acting on the smooth function in a form that is very similar to that of a local pseudopotential. This gives the method the advantage over the OPW method that it can easily be introduced into pseudopotential based methods.

The operators \tilde{A} working on the smooth pseudo wavefunction is given by:

$$\tilde{A} = T^\dagger \hat{A} T \quad (2.44)$$

Here \hat{A} denotes the original operator and \dagger denotes the hermitian conjugate operator.[20]

Ultrasoft pseudopotentials

The ultrasoft pseudopotential was proposed as a method of creating pseudopotentials that are as smooth as possible. In order to achieve this the criterion that the total charge inside the core region (the part to the left of the dotted line in figure 2.7) should be the same for the real system and the pseudo system is lifted. When the charge inside the core region is changed so is the physics of the problem, in order to correct for this an auxiliary function is introduced around the core and an overlap operator is introduced. The introduction of these functions leads to a generalized eigenvalue problem given by:

$$(\hat{H} - \varepsilon_i \hat{S}) |\psi_i\rangle = 0 \quad (2.45)$$

where ψ_i is the pseudopotential and \hat{S} is the overlap operator that is unit outside core region. S is given by:

$$\hat{S} = \hat{1} + \sum_{s,s'} \Delta Q_{s,s'} |\beta_s\rangle \langle \beta_{s'}| \quad (2.46)$$

where ΔQ is a function that describes deviation from the conserving of electrical charge and the β functions are a form of projector functions. The advantage of the ultrasoft formulation is that the the pseudo wavefunctions ψ_i can be created independently and that a low cutoff energy can be used due to the soft nature of the pseudo wavefunctions. The trade off is that more complicated Hamiltonian like equation is needed. However this is not a large problem when implemented in numerical methods.[21, 12]

Part II:

Method ,Results and Discussion

3. Project

3.1 Computational Details

Electronic proprieties of different materials have been calculated in this project: e.g. band structures, density of states and the lattice parameters. The considered systems include 3 test structures: Si as a bulk example and graphene and hexagonal boron nitride as 2D-systems. All calculations have been preformed under the framework of DFT as implemented in Quantum Espresso using pseudopotentials taken from Quantum espresso homepage or generated using Pslibrary[22]. For all cases except silicon, the pseudopotentials are of the form of generalized-gradient approximation developed by Perdew-Burke-Ernzerhof (PBE). When performing calculations on the TMD systems (i.e. MoS₂ , WTe₂) four different pseudopotentials where used: scalar relativistic (SR) and fully relativistic (FR) versions of both Projector augmented wavefunctions (PAW) and ultrasoft pseudopotentials(US).

The method used for calculations of band structure and material parameters can be divided into a set up part consisting of two steps and then the actual calculations .

The first thing that has been done is to decide the appropriate values for the cutoff energy and the Brillouin zone sampling. This has been done by varying the parameters and performing self consistent calculations in order to get a converged minimum for the total energy. After this, the structure is relaxed which has either been done by manually varying lattice parameters and finding the lattice parameter that corresponds to a minimum total energy or by using Quantum espressos Variable Cell-relax function (VC-relax) .

After that the calculations have been performed following the scheme in figure 3.1.

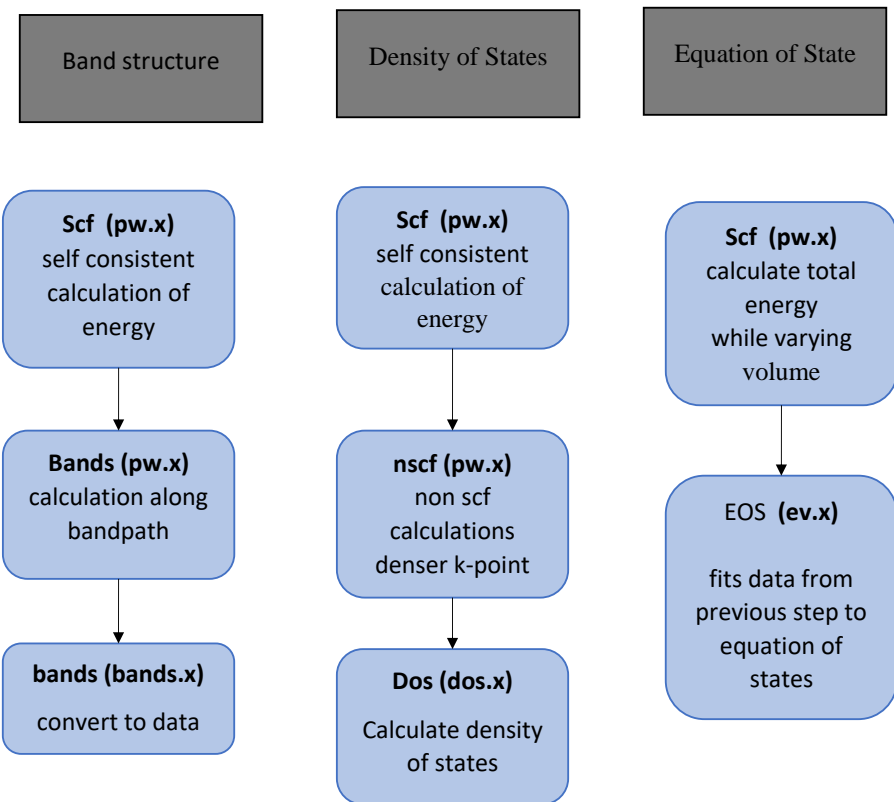


Figure 3.1. Scheme for calculations preformed with QE. grey boxes denote what is calculated. The first word is what kind of calculation is preformed and the name inside the function is the QE function used.

3.2 Quantum Espresso and Pslibrary

Quantum espresso

Quantum Espresso is a suite of open-source computer programs for calculation and modeling of materials parameters. These programs are based on DFT utilizing planewaves and pseudopotentials. Quantum Espresso is developed around the two main programs **Pwscf**, used to perform self consistent calculations and **CP** used for performing molecular dynamics calculations. The Quantum Espresso project allows the inclusion of modules developed by scientist in the field. [23]

Pslibrary

Pslibrary is an open library that allows for the creation of pseudopotentials by using Quantum espressos ld1.x function. It has support for the creation of PAW and US pseudopotentials, both scalar relativistic and fully relativistic¹ pseudopotentials [22].

3.3 Test systems

In the beginning off the project some trial systems were chosen in order to learn how to perform electronic structure calculations with Quantum Espresso.

3.3.1 Si

To start, calculations were performed on a simple three dimensional system of silicon using a simple norm-conserving non relativistic pseudopotential. The crystal structure of Si is diamond cubic crystal structure belonging to the point group (Pm-3n (223)), as shown in figure 3.2

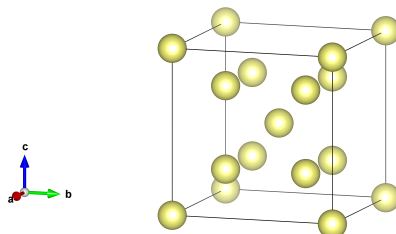


Figure 3.2. The Crystal structure of Si in a conventional unit cell. the visualization of the crystal structure was created using VESTA [24]

¹ Fully relativistic pseudopotentials incorporate the effects of spin-orbit coupling unlike scalar relativistic pseudopotentials

Before performing a band structure calculation a suitable cutoff energy and k-point mesh need to be decided. The convergence calculations are done by making a series of calculations for the total energy while varying either the cutoff energy or the number of k-points. The total energy is then plotted against the cutoff energy or the k-point mesh generating a curve that converges towards some constant value as in figure 3.3(a). and 3.3(b)

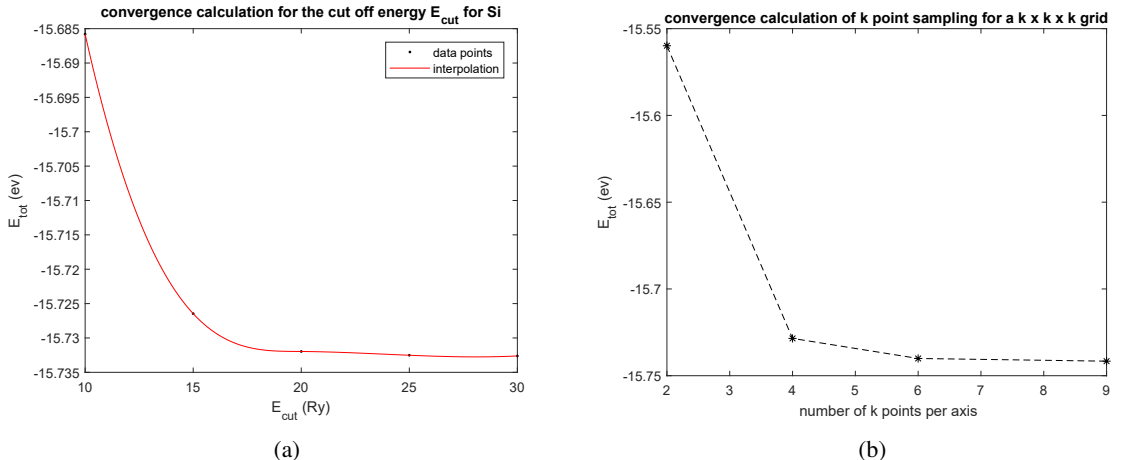


Figure 3.3. (a) Convergence calculation for the cutoff energy of Si, The black dots are the calculated data points and the red line is a fitted line. The line was fitted using matlab's spline function for cubic splines (b) convergence calculation for k-points, the * are the calculated data points and the dash line is plotted to increase visibility

For the band structure calculation, a cutoff energy of $E_{cut} = 25$ Ry and a k-point mesh of $6 \times 6 \times 6$ points were chosen.

In order to set up for the band structure calculations the structure of the system needs to be relaxed i.e. find the structural parameters that minimize stress and total energy for the unit cell. As mentioned before this can be done in two ways, but for simpler systems it can be done in a manner similar to that of the convergence calculations by varying the lattice parameter. The relaxation calculations gives graphs that looks similar to figure 3.4. And the equilibrium lattice parameter was found to be 5.477 \AA

After performing set up calculations the band structure of Si was performed along the path $R - \Gamma - X$ in the Brillouin zone for the calculations the relaxed lattice parameter a was used, as well as the converged values for the cutoff energy and k-point sampling as given above.

The bandgap between the valence band maximum (VBM) and the conduction band minimum (CBM) was found to be 0.7817 eV that pretty large deviation from the experimental can be compared to the literature value of 1.107 eV

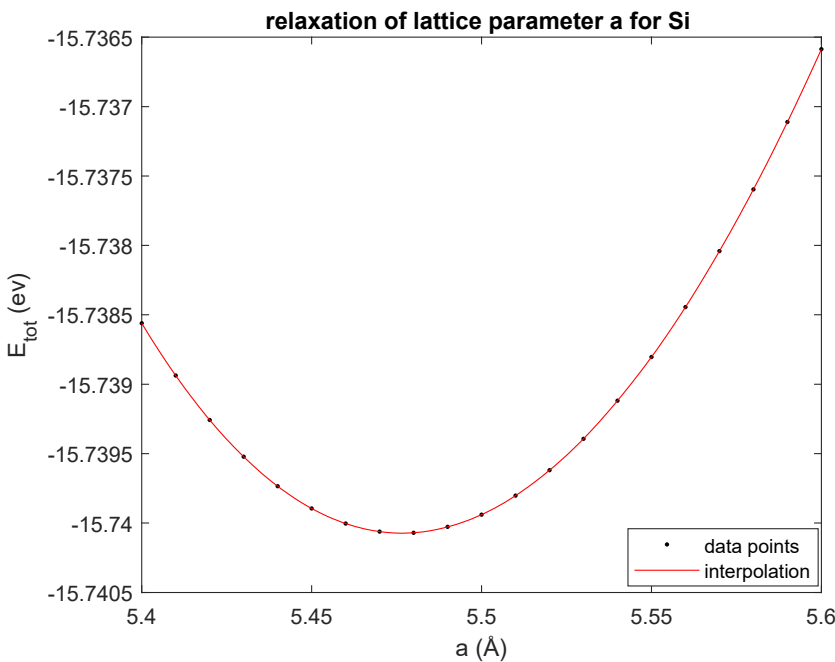


Figure 3.4. Relaxation calculation for Si system, data points are plotted as black points. The relaxed lattice parameter is the value that yields the lowest total energy

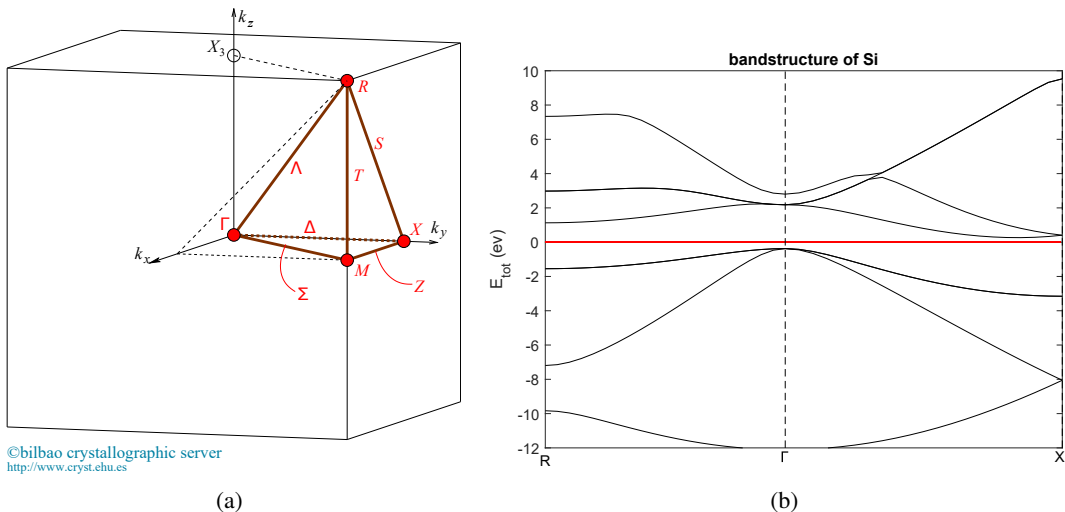


Figure 3.5. (a) shows a sketch of the first Brillouin for the Si system. (b) shows the bandstructure of Si calculated along high symmetry lines between the points $R - \Gamma - X$ seen in fig(a). Figure (a) was taken from [9].

3.3.2 Graphene

The next system considered was graphene as a simple 2D system. Graphene has a hexagonal crystal structure shown in figure 3.6. For the calculations, an ultrasoft scalar relativistic pseudopotential (US (SR)) was used taken from those available at Quantum Espressos homepage. For the calculations on

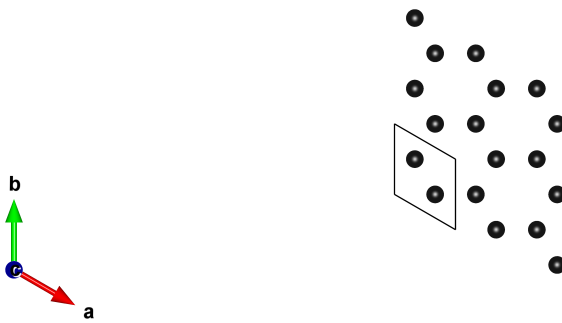
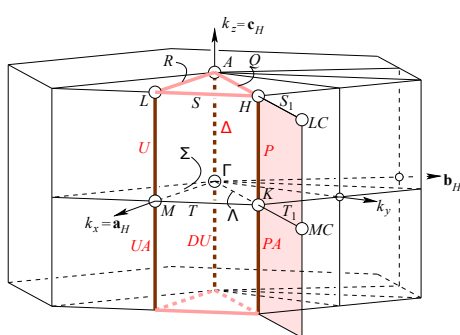


Figure 3.6. The Crystal structure of graphene as seen from above

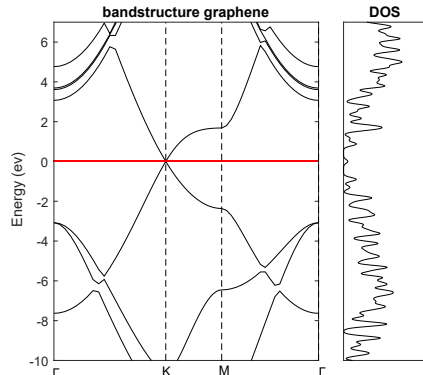
graphene, a mesh of $9 \times 9 \times 1$ k-points was used, the cutoff energy was taken to be 28 Ry and the relaxed lattice constant in the plane was found to be 2.463 Å. These values were calculated using the same methods as for the Si-system.

The band structure calculations were taken along the path $\Gamma - K - M - \Gamma$ in the first Brillouin zone. The band structure was calculated using the general method from figure 3.1. The k-point mesh for non self consistent calculations (ncsf) was taken to be $18 \times 18 \times 2$. and a smearing of 0.01 eV was used. The results are shown in figure 3.7, where it can be seen that graphene is a semimetal where valence and conduction bands cross linearly at the Dirac point at the Fermi level at \mathbf{K} .



©bilbao crystallographic server
<http://www.cryst.ehu.es>

(a)

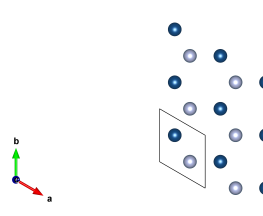


(b)

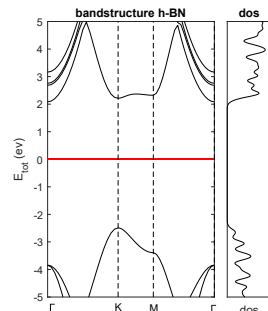
Figure 3.7. (a) shows the Brillouin zone for an hexagonal system. figure (b) shows the calculated band structure and DOS for graphene. Fig (a) taken from [9]

3.3.3 Hexagonal Boron Nitride

The next system that was considered was a monolayer of hexagonal boron nitride (h-BN). h-BN is structurally very similar to graphene, it has the same lattice structure but the carbon atoms are replaced by boron and nitrogen atoms. Since the underlying lattice is the same as for graphene and h-BN has the same form of first Brillouin zone The band structure was calculated along the same path as for graphene. The calculations were performed using a $9 \times 9 \times 1$ grid for a cutoff energy of 32 Ry. The relaxed lattice parameter was found to be 2.5082 Å. The bandgap for the h-BN system was calculated from fig 3.8(b) and was found to be 4.6 eV.



(a)



(b)

Figure 3.8. (a) The Crystal structure of hexagonal boron nitride where the blue atoms are boron atoms and the grey atoms are nitrogen. (b) Band structure and density of states for monolayer of hexagonal Boron Nitride calculated using US pseudo potentials with SR data sets. the Fermi energy is plotted as red line and has been taken to be zero.

Hexagonal Boron nitride and graphene are structurally very similar. They have as said the same crystal structure and the same total number of electrons. However, the electronic structures of the systems are very different due to their different chemical species. The calculated value for the band gap captures this difference, however compare to the real value of approximately 6 eV [25] it is a rather large underestimation, which is expected for PBE.

3.4 TMDs

A lot of interest has been taken in the TMDs and in particular in monolayers of TMDs. The TMDs show a wide variation in electrical properties and there are many proposed applications for these materials. The TMDs consist of layered structures where the different layers are held together by weak Van der Waals forces.

3.4.1 Tungsten ditelluride (WTe_2)

Bulk WTe_2 consist of layered sheets of WTe_2 and the stable form has an orthorombic crystal structure. The crystal structure of a single layer together with the stacking order of bulk tungsten ditelluride is shown in figure 3.4.1. The relaxed crystal structure was obtained using Quantum espressos VC-relax function. VC-relax is a function that minimizes the force and stress in the system using a iteration of self consistent calculations while adapting the lattice parameters and ion positions. The calculated lattice parameters are shown in table 3.1 and 3.2. The values obtained are a very good match for the in plane lattice parameters, however there is a rather large discrepancy for the values of out of plane lattice parameter compared with that of the experimental. This is probably due to the fact that the unit cell was created with a bit to large value to start with.

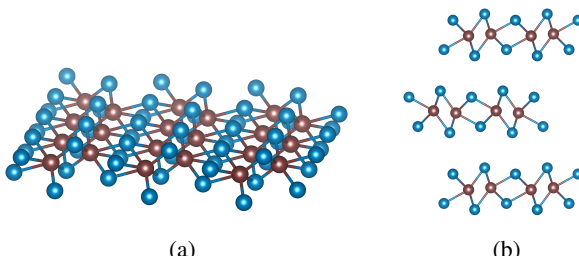


Figure 3.9. (a) Monolayer of WTe_2 , Where the brown atoms represent tungsten and the blue atoms represent Telluride. (b) shows a sideways view of the stacking order used for Bulk WTe_2 . Figure (a) and (b) was created using VESTA [24].

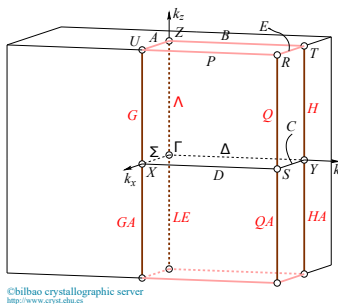


Figure 3.10. The Brillouin zone for orthorhombic WTe_2 , taken from [9]

Bulk WTe_2

| Pseudopotential | a [\AA] | b [\AA] | c [\AA] |
|-----------------|----------------------|----------------------|----------------------|
| US (SR) | 3.54 | 6.24 | 13.75 |
| US (FR) | 3.50 | 6.28 | 15.43 |
| PAW (SR) | 3.54 | 6.24 | 13.75 |
| PAW (FR) | 3.54 | 6.28 | 15.43 |
| exp | 3.50 | 6.28 | 14.07 |

Table 3.1. Calculated lattice parameters for Bulk WTe_2 . The values were obtained by performing a VC-relax calculation with Quantum Espresso. a b c are the lattice parameters, describe in section 2.2.1 . In the table the pseudopotentials are denoted by the shortened form used in this report: e.g. the ultrasoft scalar relativistic pseudopotential is denoted US (SR). The experimental values are taken from [26]

Monolayer WTe_2

| Pseudopotential | a [\AA] | b [\AA] | c [\AA] |
|-----------------|----------------------|----------------------|----------------------|
| US (SR) | 3.51 | 6.28 | 13.3 |
| US (FR) | 3.50 | 6.28 | 15.4 |
| PAW (SR) | 3.50 | 6.28 | 15.4 |
| PAW (FR) | 3.50 | 6.28 | 15.4 |
| exp | 3.50 | 6.28 | - |

Table 3.2. Calculated lattice parameters for monolayers WTe_2 . The values were obtained by performing VC-relax calculations with Quantum Espresso. a b c are the lattice parameters, describe in section 2.2.1 . In the table the pseudopotentials are denoted by the shortened form used in this report: e.g. the ultrasoft scalar relativistic pseudopotential is denoted US (SR), The experimental values are taken from [26]

Bulk

The band structure calculations for WTe_2 were performed along the $Y - \Gamma - X$ path in the Brillouin zone of WTe_2 (a schematic of the Brillouin zone can be seen in figure 3.4.1). In the calculations a k-point mesh of $8 \times 4 \times 2$ points were used and the cutoff energy was taken to be 60 Ry. The values for cutoff energy and k-point mesh were calculated separately, for each of the pseudopotentials. The relaxed lattice parameters were obtained by using vc-relax for each of the calculations the Van der Waals interaction was included using the dft-d correction.

By comparing the band structure of the fully relativistic pseudopotential and the scalar relativistic pseudopotentials the effect of spin-orbit coupling can be seen: the splitting of the bands are most apparent in lower right corner. This effect is expected to be quite large for WTe_2 since the strength of spin orbit coupling increases as the atoms gets heavier. The effects around the Fermi energy are however very small as can be seen in from the DOS having the same characteristic around the Fermi energy.

Monolayer of WTe_2

The monolayer structure of tungsten ditelluride was created with a vertical gap of roughly 12 Å between unitcells, in order to separate each layer from its periodic image in the vertical direction. For the calculations a k-point mesh of $8 \times 4 \times 2$ k-points were used and a cutoff energy of 60 Ry. These were obtained for each of the pseudo potentials separately using the same method as was used for the silicon system. The relaxed parameters were obtained using VC-relax calculations in Quantum espresso.

For the case of monolayer WTe_2 the number of bands in the plot are much lower than for that of Bulk WTe_2 this is due to the fact that the number of electrons in the unit cell is much lower for the case of monolayer compared with bulk. For the monolayer there are no splitting in the bands due to the spin-orbit coupling as compared with the splitting that occurs in bulk. This is however expected since the crystal structure of monolayer WTe_2 has inversion symmetry [27]. One point of interest in the band structure is at the Γ point where a small pocket is formed in the where the Fermi energy intersect the valence band. This pocket can be seen in figure 3.12(a). This effect is present in the other band structures. However it is almost not visible in figure 3.12. It is possible these effect could have been seen if a higher cut off energy and a larger amount of k-points were used since the values chosen for the calculations was on the smaller side.

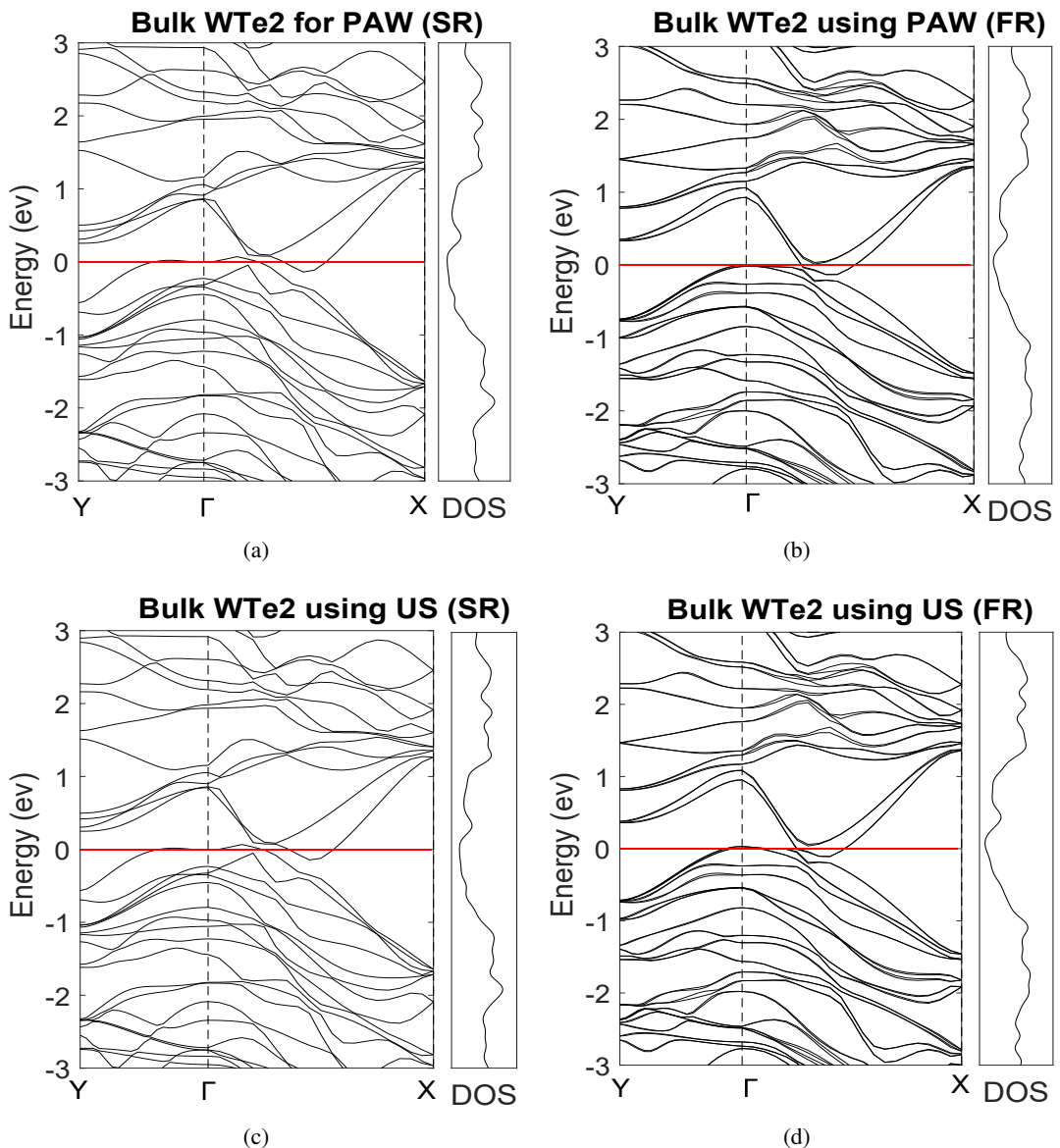


Figure 3.11. The calculated band structure and DOS for Bulk of WTe₂ (a) Shows the band structure calculated using a scalar relativistic PAW pseudopotential. (b) Shows the band structure calculated using a fully relativistic PAW pseudopotential. (c) Shows the band structure calculated using a scalar relativistic Ultrasoft pseudopotential. (d) Shows the band structure calculated using a fully relativistic Ultrasoft pseudopotential.

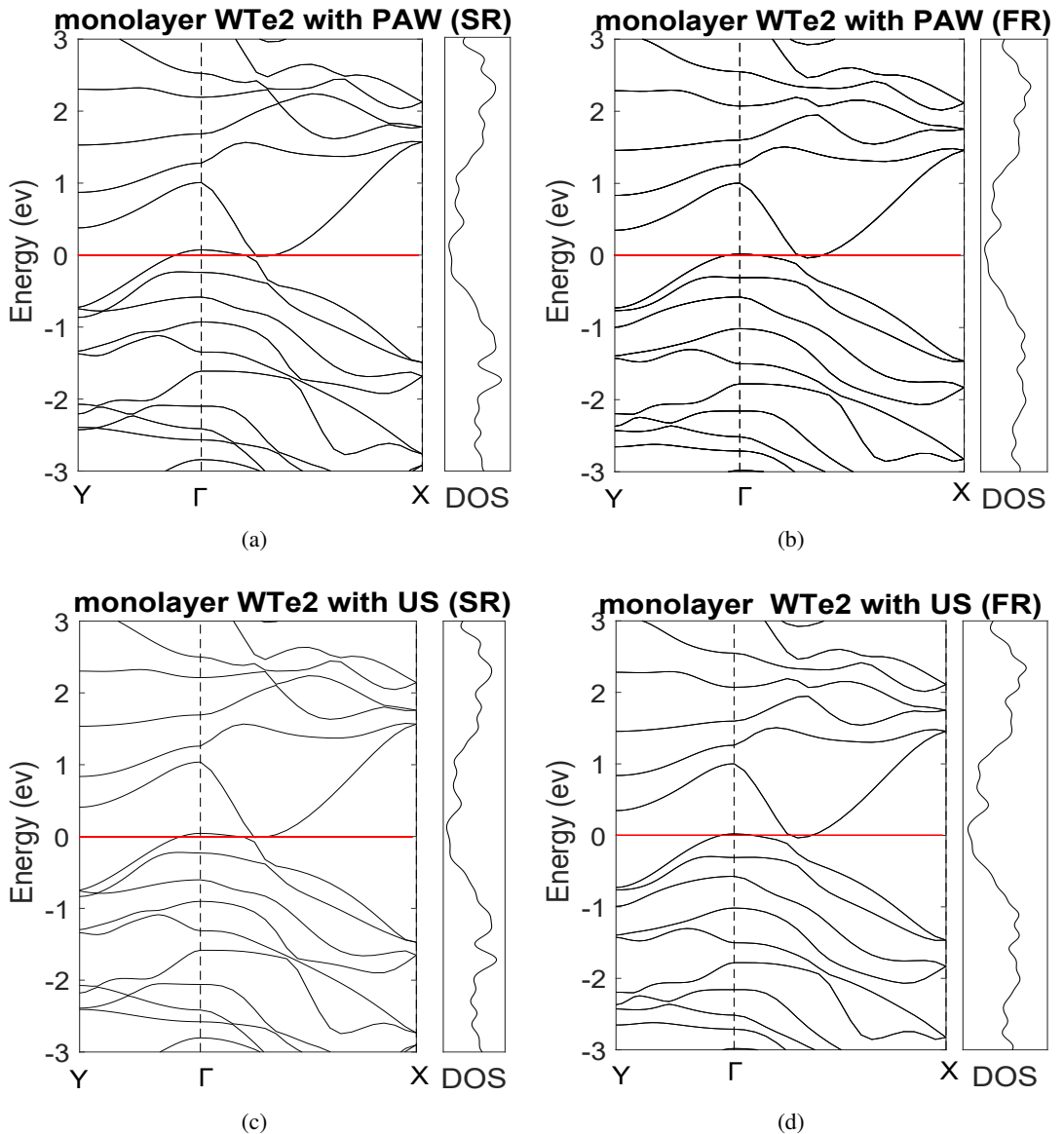


Figure 3.12. The calculated band structure and DOS for monolayer of WTe₂ (a) Shows the band structure calculated using a scalar relativistic PAW pseudopotential. (b) Shows the band structure calculated using a fully relativistic PAW pseudopotential. (c) Shows the band structure calculated using a scalar relativistic ultrasoft pseudopotential. (d) Shows the band structure calculated using a fully relativistic ultrasoft pseudopotential.

3.4.2 MoS₂

MoS₂ is a layered material that consists of hexagonal sheets stacked on top of each other connected by van der Waals interactions. Due to its hexagonal structure, MoS₂ has the same Brillouin zone as that of graphene and h-BN. (See fig: 3.7(a))

The energy cutoffs used in the calculations were chosen to have high values to ensure that the pseudopotentials worked well. The high cut off energy was chosen in order to be well above the suggested minimum cutoffs of the pseudopotentials. The cutoff energies used are approximately 60 Ry, which is comparably large to other values used in similar computations seen in the literature, cut offs obtained can there for be trusted to be converged.

Monolayer

For the crystal structure of monolayer MoS₂, a vertical spacing of approximately 15 Å was used in between layers. For the calculations, a k-point mesh of $9 \times 9 \times 3$ was used for all the different pseudopotentials. For the US pseudopotentials, a 60 Ry cutoff energy was used and for the PAW, a 65 Ry cutoff energy. The band structure was calculated along the $\Gamma - M - K - \Gamma$ path in the Brillouin zone(See 3.7(a)). The bandgap was then calculated by measuring the difference between the valence band maximum (VBM) and the conduction band minimum (CBM) where the calculated values are shown in table 3.3.

The relaxed values for the lattice parameter a was calculated using the same method as for the silicon system. For the case of monolayer MoS₂, the out-of-plane lattice value was kept constant while a was varied. The obtained values for the lattice parameter are tabulated in table 3.3. The obtained values overestimate the lattice parameter by approximately 1%. This is expected as GGA is known to overestimate the lattice parameter. The underestimation of the bandgap is also in accordance with what is expected.

The band structures in figure 3.14 are pretty similar, however when spin-orbit-coupling is not included the band gap is not properly recovered, as can be seen in figure 3.14. The band gaps for the scalar relativistic pseudopotentials are indirect going between the Γ point and K point. However monolayer MoS₂ is known a have a direct band gap at the k-point. This behaviour is properly described when including spin-orbit coupling.

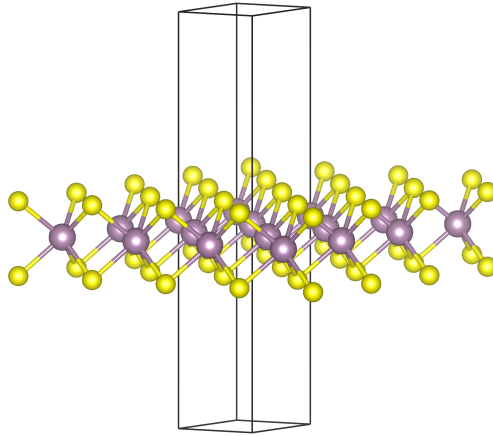


Figure 3.13. A monolayer of MoS_2 where the S atoms are shown as yellow balls and the Mo atoms are shown as purple balls. The box shown in the picture shows the extension of the unit cell. The representation of monolayer MoS_2 was created using VESTA [24]

| Monolayer MoS_2 | Pseudopotential | $a [\text{\AA}]$ | Bandgap [eV] |
|--------------------------|-----------------|------------------|--------------|
| US (SR) | | 3.18 | 0.81 |
| US (FR) | | 3.19 | 1.63 |
| PAW (SR) | | 3.19 | 1.10 |
| PAW (FR) | | 3.20 | 1.46 |
| Experimental | | 3.16 | 1.8 |

Table 3.3. Calculated lattice parameters for monolayer of MoS_2 . The values were obtained by the method described for the silicon system. The table is ordered by the pseudopotential used in the calculation. The experimental values of the lattice constant was taken from [28] and the experimental value of the bandgap from [29].

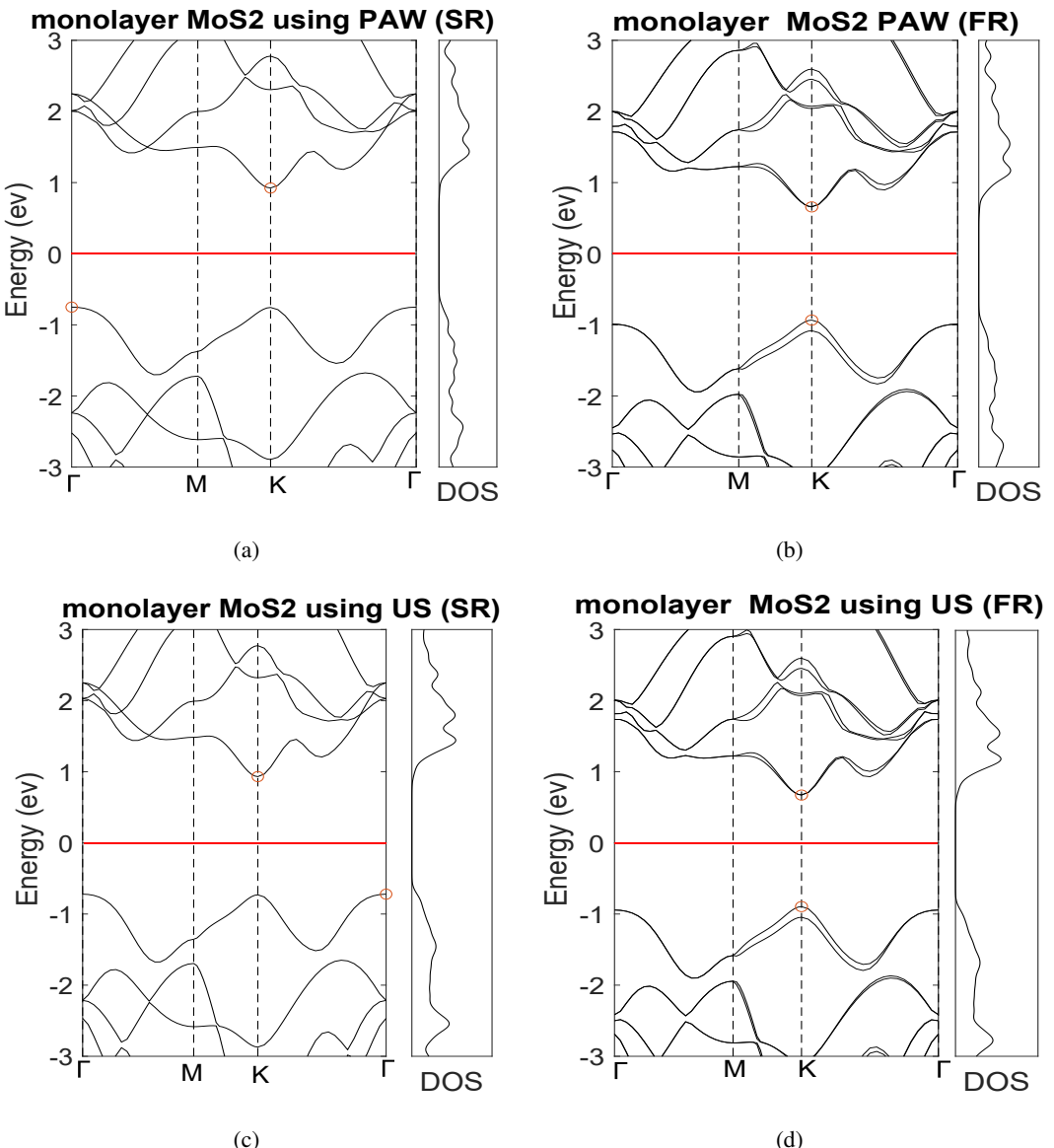


Figure 3.14. The calculated band structures and DOS for monolayer of MoS₂. The valence band maximum and conduction band minimum is shown as orange circles. The Fermi energy is taken to be zero and shown as a red line. (a) Shows the band structure calculated using a scalar relativistic PAW pseudopotential. (b) Shows the band structure calculated using a fully relativistic PAW pseudopotential. (c) Shows the band structure calculated using a scalar relativistic ultrasoft pseudopotential. (d) Shows the band structure calculated using a fully relativistic ultrasoft pseudopotential.

Bilayer

For the Bilayer of MoS₂, a stacking called AA' was used. The stacking is obtained by placing Mo atoms above S atoms and S atoms above Mo as in figure 3.15(b). A vertical spacing of 12 Å was used in the calculational unit cell to separate the periodic images. For the ultrasoft pseudopotentials a k-point mesh of 9×9×2 points were used together with a 70 Ry cutoff energy. For PAW pseudopotentials a k-point mesh of 6×6×1 and a cutoff energy of 65 Ry were used. The lattice parameters were calculated using VC-relax and the obtained values are shown in table 3.4.

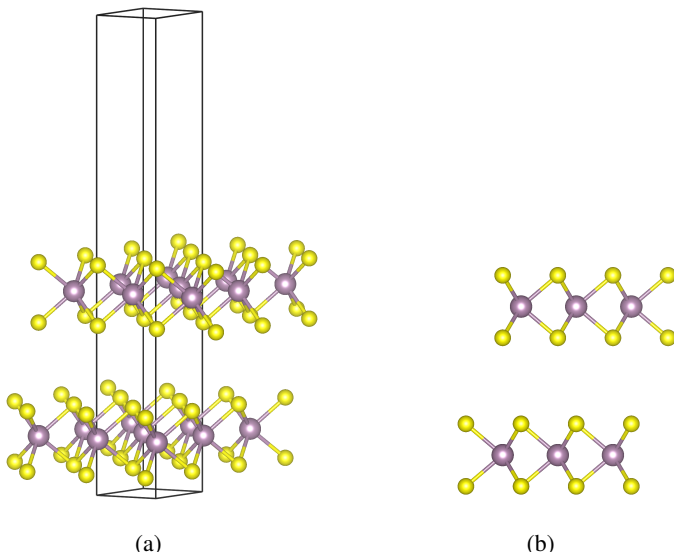


Figure 3.15. (a) Bilayer MoS₂ where Mo is shown as purple balls, S is shown as yellow balls. The rectangular box shows how large the spacing was taken between bilayers. (b) Shows the AA' stacking used for the bilayer structure. Figure (a) and (b) was created using VESTA [24]

For the Bilayer system the bandgap is changed from a direct bandgap at K to a indirect bandgap between the K and Γ points, as can be seen in figure 3.16. The bandstructures are also very similar and there is no splitting due to spin orbit coupling. This is due to the fact that degeneracy is not lifted for systems with space inversion symmetry. So since the Bilayer has space inversion symmetry there should be no splitting in the bands due to spin-orbit coupling.

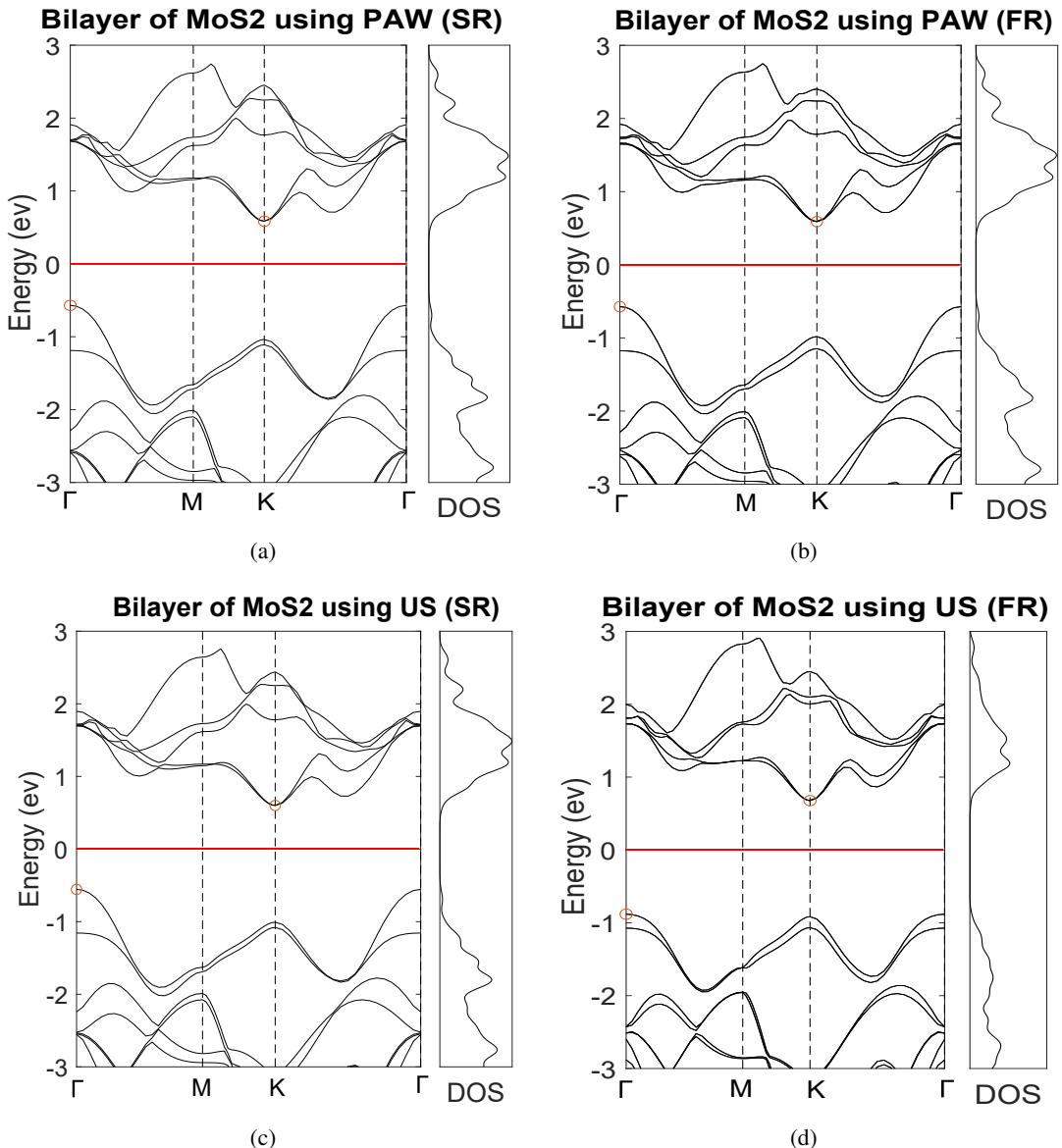


Figure 3.16. The calculated band structure and DOS for Bilayer of MoS_2 . The valence band maximum and conduction band minimum are shown as orange circles. The Fermi energy is taken to be zero and shown as a red line. (a) Shows the band structure calculated using a scalar relativistic PAW pseudopotential. (b) Shows the band structure calculated using a fully relativistic PAW pseudopotential. (c) Shows the band structure calculated using a scalar relativistic ultrasoft pseudopotential. (d) Shows the band structure calculated using a fully relativistic ultrasoft pseudopotential.

| Bilayer MoS ₂ | | |
|--------------------------|--------|--------|
| Pseudopotential | a [Å] | c [Å] |
| US (SR) | 3.20 | 21.7 |
| US (FR) | 3.19 | 24.9 |
| PAW (SR) | 3.19 | 21.4 |
| PAW (FR) | 3.19 | 24.9 |

Table 3.4. calculated lattice parameters for bilayers of MoS₂. The values were obtained by using Quantum Espressos VC-relax function.

Trilayer

The crystal structure used for the trilayer is shown in figure 3.17. The computational unit cell that was used for the trilayer systems was created with a vertical space of approximately 12 Å between the images. For the calculations a mesh of $9 \times 9 \times 2$ k-points where chosen for all pseudopotentials. For the calculations using the SR US pseudopotential a 65 Ry energy cutoff was chosen while for the FR US and the PAW pseudopotentials a 60 Ry energy cutoff was chosen. The relaxed lattice parameters where calculated using VC-relax and are shown in table 3.5.

The calculated band structure are very similar to that of the bilayer MoS₂ the indirect band gap between the Γ and K points. However unlike in the case of the bilayer the band structure is affected by spin orbit coupling as can be seen in 3.25, since there is no inversion symmetry.

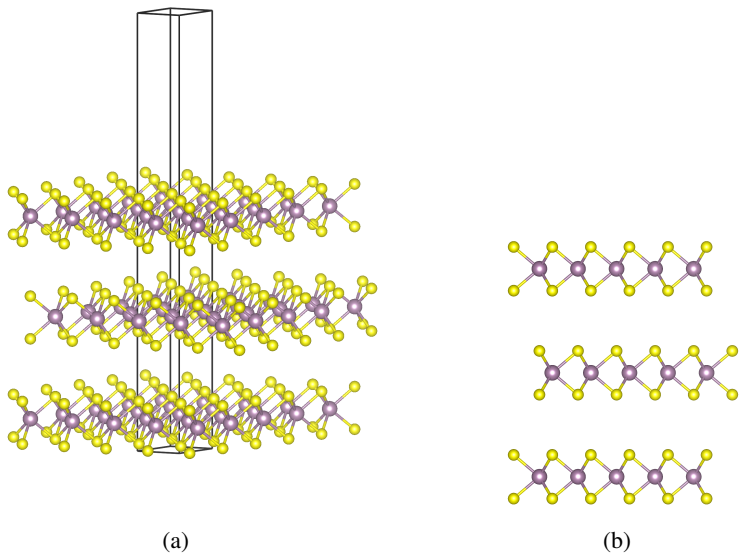


Figure 3.17. (a) Trilayer of MoS₂ where the Mo atoms are purple , the Si atoms are yellow. The box in the picture shows the extension of the unit cell . 3.17(b) shows the stacking of the three layers from the side. Figure (a) and 3.17(b) was created using VESTA [24].

| Trilayer MoS ₂ | Pseudopotential | a [Å] | c [Å] |
|---------------------------|-----------------|--------|--------|
| US (SR) | | 3.20 | 27.3 |
| US (FR) | | 3.19 | 32.2 |
| PAW (SR) | | 3.19 | 27.2 |
| PAW (FR) | | 3.19 | 32.2 |

Table 3.5. calculated lattice parameters for Trilayers of MoS₂. The values where obtained by using Quantum Espresso VC-relax function. The table is ordered by the pseudopotential used in the calculation.

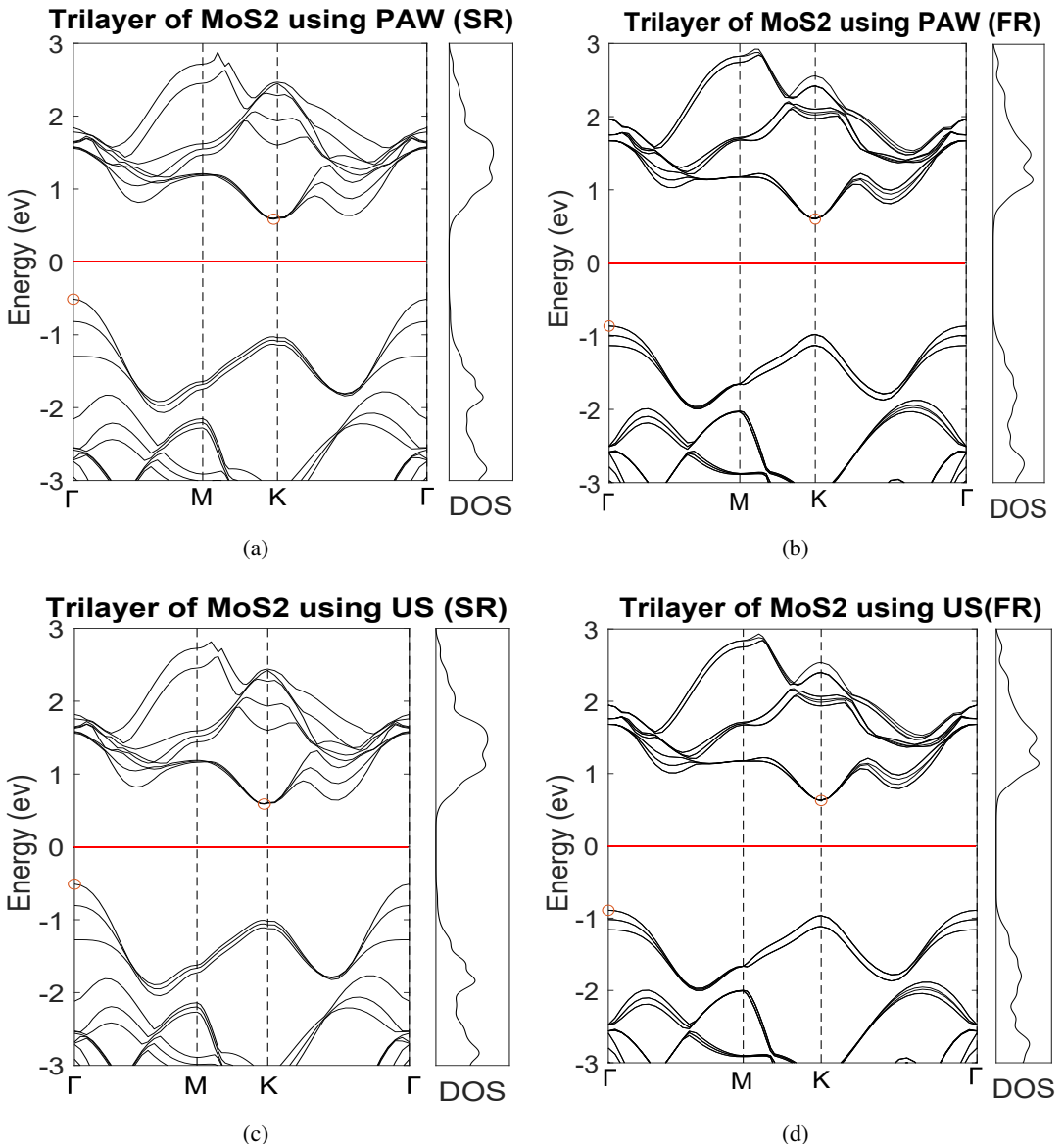


Figure 3.18. The calculated band structure and DOS for Trilayer of MoS₂. The valence band maximum and conduction band minimum are shown as orange circles. The Fermi energy is taken to be zero and shown as a red line. (a) Shows the band structure calculated using a scalar relativistic PAW pseudopotential. (b) Shows the band structure calculated using a fully relativistic PAW pseudopotential. (c) Shows the band structure calculated using a scalar relativistic ultrasoft pseudopotential. (d) Shows the band structure calculated using a fully relativistic ultrasoft pseudopotential.

Bulk

For the bulk MoS₂, a kpoint mesh of $15 \times 15 \times 3$ was used for the ultrasoft pseudopotentials and a mesh of $9 \times 9 \times 2$ was used for the PAW pseudopotentials. For all of the pseudopotentials, a cutoff energy of 60 Ry. was used. The relaxed lattice parameters were calculated using Quantum Espressos VC-relax function. The band structure was then calculated along the $\Gamma - M - K - \Gamma$ path using the relaxed parameters. After preforming the band structure calculations the bandgap was calculated by taking the difference between the CBM and VBM and the results are includeed in tabel 3.6.

In the band structure of bulk MoS₂ the CBM at K has been replaced by a new CBM at point halfway between the K and Γ points. The progressive lowering of the bands halfway Γ and K when the number of layers is increased can be seen by comparing the development of the CBM for scalar relativistic pseudopotential in figures 3.14, 3.16 and 3.25.

There are again only small difference between the fully relativistic and scalar relativistic versions this is again due to the fact that the bulk system has a space inversion symmetry. so no splitting in the bands are expected.

The calculated lattice parameters and band gaps are a good fit with the experimental data, considering that the band gaps are expected to be under estimated. due to the use of PBE exchange-correlation functional.

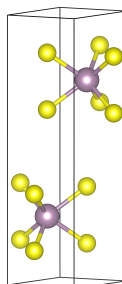


Figure 3.19. Unit cell of bulk MoS₂ where Mo atoms are shown as purple balls , S atoms are shown as yellow balls. The figure of the unit cell was created using VESTA [24].

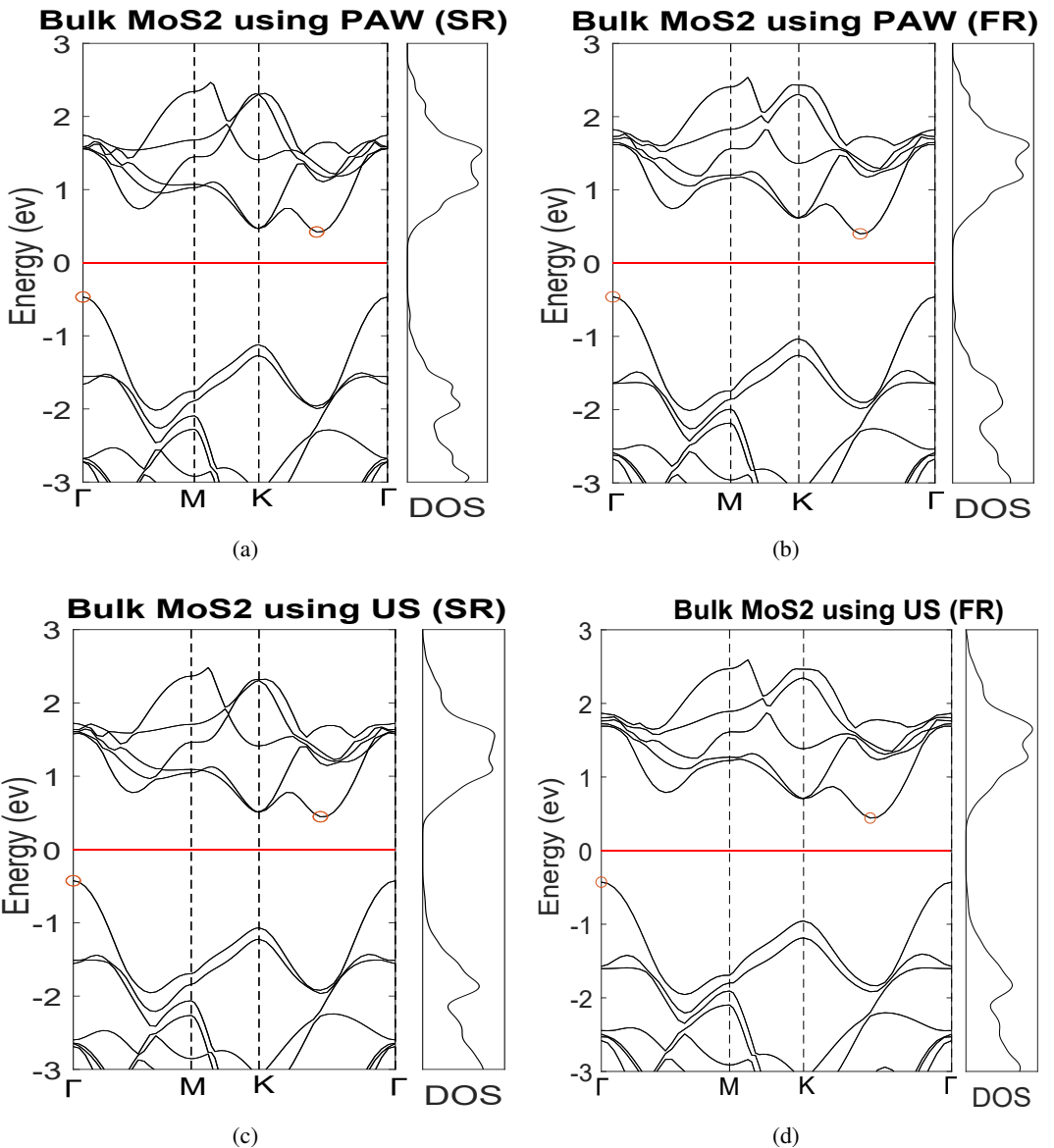


Figure 3.20. The calculated band structure and DOS for bulk MoS₂. The valence band maximum and conduction band minimum is shown as orange circles. The Fermi energy is taken to be zero and shown as a red line. (a) Shows the band structure calculated using a scalar relativistic PAW pseudopotential. (b) Shows the band structure calculated using a fully relativistic PAW pseudopotential. (c) Shows the band structure calculated using a scalar relativistic ultrasoft pseudopotential. (d) Shows the band structure calculated using a fully relativistic ultrasoft pseudopotential.

The splitting in the valence band at the K point (Δ_{VB-k}) is dependent primarily on two effects; the interlayer coupling and the intralayer spin-orbit coupling (SOC). The splittings of valence band (VB) at the K point for the calculated band structures are given in table 3.7. The splitting energies were calculated by taking the difference between the two topmost in the VB at the K-point. In the case of trilayer MoS₂ using PAW (SR) the VB is split into three different bands at the K point, for this case the splitting was calculated by taking the difference between the top and bottom of these bands.

In monolayer, splitting occurs solely due to the spin-orbit coupling, the splitting in monolayer is therefore equal to the splitting due to the intralayer SOC. The effect of the intralayer SOC is found to be 150 meV. In the bilayer, the bands of are split due to the effect of intralayer SOC and interlayer coupling. The splitting gives rise to two degenerate bands due to the symmetry of bilayer crystal structure. The splitting gets contribution from both SOC and interlayer coupling as evident from the comparison of SR and FR results. The splitting in bulk MoS₂ are due to the same effects as for bilayer. The difference between the splitting can be attributed to the increased splitting due to the interlayer coupling as the total number of layers are increased as can be seen in table 3.7.

The splitting of the VB of trilayer MoS₂ does not follow the same trend of an increased splitting with the number of layers as in the case of bilayer and bulk. this might be explained by the fact that unlike bilayer and bulk trilayer does not have an inversion symmetry. The effect of splitting from SOC can therefore be expected to differ between even and odd layers. when comparing the SR cases it is however obvious that the interlayer coupling increases in strength as the number of layers increases.

The generated results are consistent with experiments and similar calculation. [31, 32]

| Bulk MoS ₂ | | | |
|-----------------------|--------|--------|---------------|
| Pseudopotential | a [Å] | c [Å] | Band gap [ev] |
| US (SR) | 3.20 | 12.31 | 0.87 |
| US (FR) | 3.16 | 12.29 | 0.87 |
| PAW (SR) | 3.16 | 12.29 | 0.89 |
| PAW (FR) | 3.16 | 12.29 | 0.86 |
| Experimental | 3.16 | 12.295 | 1.2 |

Table 3.6. calculated lattice parameters for Bulk MoS₂. The values where obtained by using Quantum Espressos VC-relax function. The table is ordered by the pseudopotential used in the calculation. The experimental value for lattice parameters was taken from [28] and the Bandgap from [30]

| | Monolayer Δ_{VB-K} [meV] | Bilayer Δ_{VB-K} [meV] | Trilayer Δ_{VB-K} [meV] | Bulk Δ_{VB-K} [meV] |
|----------|------------------------------------|----------------------------------|-----------------------------------|-------------------------------|
| PAW (FR) | 150 | 165 | 150 | 225 |
| PAW (SR) | 0 | 73 | 103 | 148 |

Table 3.7. Calculated splitting of the valence band at the K-points, for different stackings of MoS₂. The splitting is given for the band structures obtained using the PAW pseudopotentials.

3.5 Transferability of Pseudopotentials

It is important when creating pseudopotentials that the results obtained can be trusted independent of which atomic environment the pseudopotential is used in. This means that the pseudopotentials should give accurate results independent of what system it is used in. This property of pseudopotentials are known as the transferability of the pseudopotential. In order to compare the transferability of the pseudopotentials the lattice parameters and bulk modulus was computed for Molybdenum, Tungsten and Tellurium. The Bulk modulus was calculated by fitting calculated energy vs unitcell volume to a 3rd order Birch-Murnaghan equation of state (B-M EOS). The 3rd order (B-M EOS) is given by:

$$E = E_0 + \frac{9V_0B_0}{16} \left\{ \left[\left(\frac{V_0}{V} \right)^{(2/3)} - 1 \right]^3 B'_0 + \left[\left(\frac{V_0}{V} \right)^{\frac{2}{3}} - 1 \right]^2 \left[6 - 4 \left(\frac{V_0}{V} \right)^{\frac{2}{3}} \right] \right\} \quad (3.1)$$

E_0 is the minimum energy, B_0 is the bulk modulus, V_0 is the equilibrium volume and B'_0 is the pressure derivative of the bulk modulus. [33]

3.5.1 Mo

The stable form of Molybdenum has a body centered cubic (bcc) crystal (The crystal structure is shown in figure 3.21). Before calculating the bulk modulus convergence calculations were preformed in the same way as for the silicon system. From these calculations, a mesh of $6 \times 6 \times 6$ k-points and an energy cutoff of 60 Ry was chosen for all pseudopotentials. After that the energy for different lattice volumes were calculated by varying the lattice parameter and performing self consistent calculations of the energy at each value. An equation of state was fitted to the obtained data points using Quantum Espressos "ev.x" function. The Equation of state used in these calculations were a 3:rd order Birch-Murnaghan.

| Mo | | |
|-----------------|--------------------------|--------------------|
| Pseudopotential | Lattice parameter a [Å] | Bulk modulus [GPa] |
| US (SR) | 3.17 | 265.3 |
| US (FR) | 3.17 | 264.8 |
| PAW (SR) | 3.16 | 264.2 |
| PAW (FR) | 3.16 | 265.9 |
| Experimental | 3.1470 | 265.29 |

Table 3.8. Lattice parameter and Bulk modulus of bcc Molybdenum, values were obtained from fitting to Birch 3:rd order equation of state. Experimental lattice parameters are taken from [34] and bulk modulus from [35]

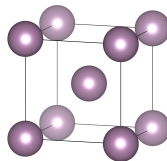


Figure 3.21. the unit cell of bulk Mo, created using the VESTA software [24]

Both the obtained lattice parameters and bulk modulus in table 3.8 and the calculated values form table 3.6, show a good agreement with experimental result, showing that at least for two simple systems the pseudopotentials obtained for molybdenum gives good results.

3.5.2 W

The stable face of Bulk Tungsten is also a bcc crystal structure. The calculations where preformed in the same way as for Molybdenum with a cutoff energy of 60 Ry and a k-point mesh of $6 \times 6 \times 6$.

The fitted values for the lattice parameter and the bulk modulus are given in table 3.9 and are very close to the experimental values.

| W | | |
|-----------------|--------------------------|--------------------|
| Pseudopotential | Lattice parameter a [Å] | Bulk modulus [GPa] |
| US (SR) | 3.18 | 319.0 |
| US (FR) | 3.18 | 326.6 |
| PAW (SR) | 3.18 | 319.7 |
| PAW (FR) | 3.18 | 319.2 |
| Experimental | 3.165 | 314.15 |

Table 3.9. Lattice parameter and Bulk modulus of bcc tungsten, values were obtained from fitting to Birch 3rd order equation of state. Experimental lattice parameters are taken from [34] and bulk modulus from [35]

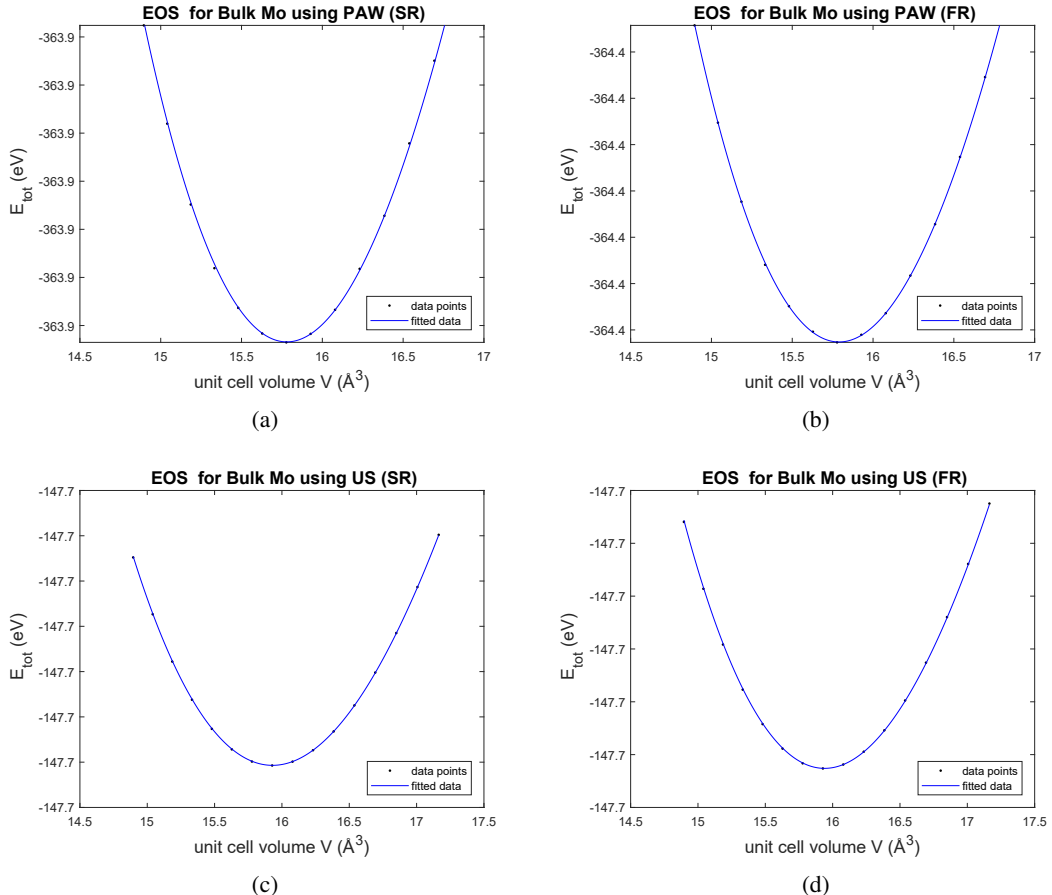


Figure 3.22. The fitted curves for the EOS of bulk Molybdenum: (a) Shows the data point and fit for scalar relativistic PAW pseudopotential. (b) Shows the data point and fit for fully relativistic PAW pseudopotential. (c) Shows the data point and fit for scalar relativistic ultrasoft pseudopotential. (d) Shows the data point and fit for fully relativistic ultrasoft pseudopotential.

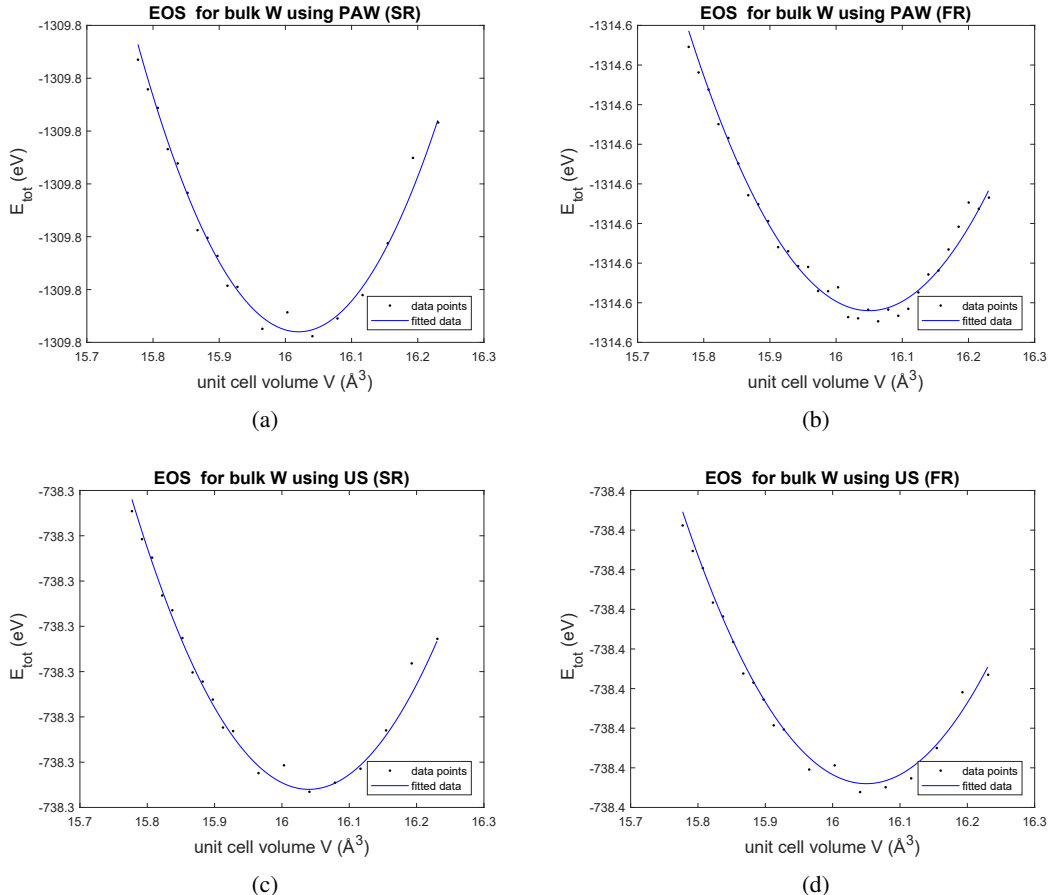


Figure 3.23. Calculated data points and fitted curves for the EOS of bulk Tungsten: (a) Shows the data point and fit for scalar relativistic PAW pseudopotential. (b) Shows the data point and fit for fully relativistic PAW pseudopotential. (c) Shows the data point and fit for scalar relativistic ultrasoft pseudopotential. (d) Shows the data point and fit for fully relativistic ultrasoft pseudopotential.

3.5.3 Te

Te in its trigonal crystal structure was considered. For the calculations a $6 \times 6 \times 6$ k-point mesh was used together with 60 Ry cut energy. The lattice parameters were obtained by performing VC-relax calculations as done for the TMDs when calculating band structure. The volume was then calculated chaining the volume while keeping the ratio of $\frac{c}{a}$ constant. The ratio of $\frac{c}{a}$ was taken to be the same as for the relaxed system. After the data points for the volume energy curve had been calculated we used ev.x to fit parameters to a 3:rd order Birch-Murnaghan. As can be seen in table 3.10 the calculated values of the bulk modulus deviates very much from the experimental value. It is unclear why this is the case however it is consistent with what other similar calculations[36],

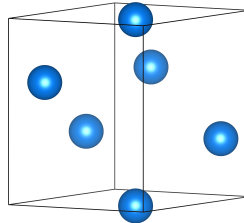


Figure 3.24. Unit cell of trigonal Te, created using VESTA [24]

| Te | Pseudopotential | a [Å] | b [Å] | c [Å] | γ [°] | B [GPa] |
|--------------|-----------------|--------|--------|--------|--------------|---------|
| US (SR) | | 4.32 | 4.30 | 6.03 | 119 | 45.2 |
| US (FR) | | 4.46 | 4.46 | 5.93 | 120 | 43.6 |
| PAW (SR) | | 4.32 | 4.30 | 6.04 | 119 | 45.2 |
| PAW (FR) | | 4.46 | 4.46 | 5.93 | 120 | 43.5 |
| Experimental | | 4.457 | 4.457 | 5.926 | 120 | 24 |

Table 3.10. Lattice parameter and Bulk modulus of trigonal Tellurium, values for lattice parameters were obtained from VC-relax calculations and the bulk modulus from fitting to Birch 3rd order equation of state. Experimental lattice parameters are taken from [34] and bulk modulus from [37]

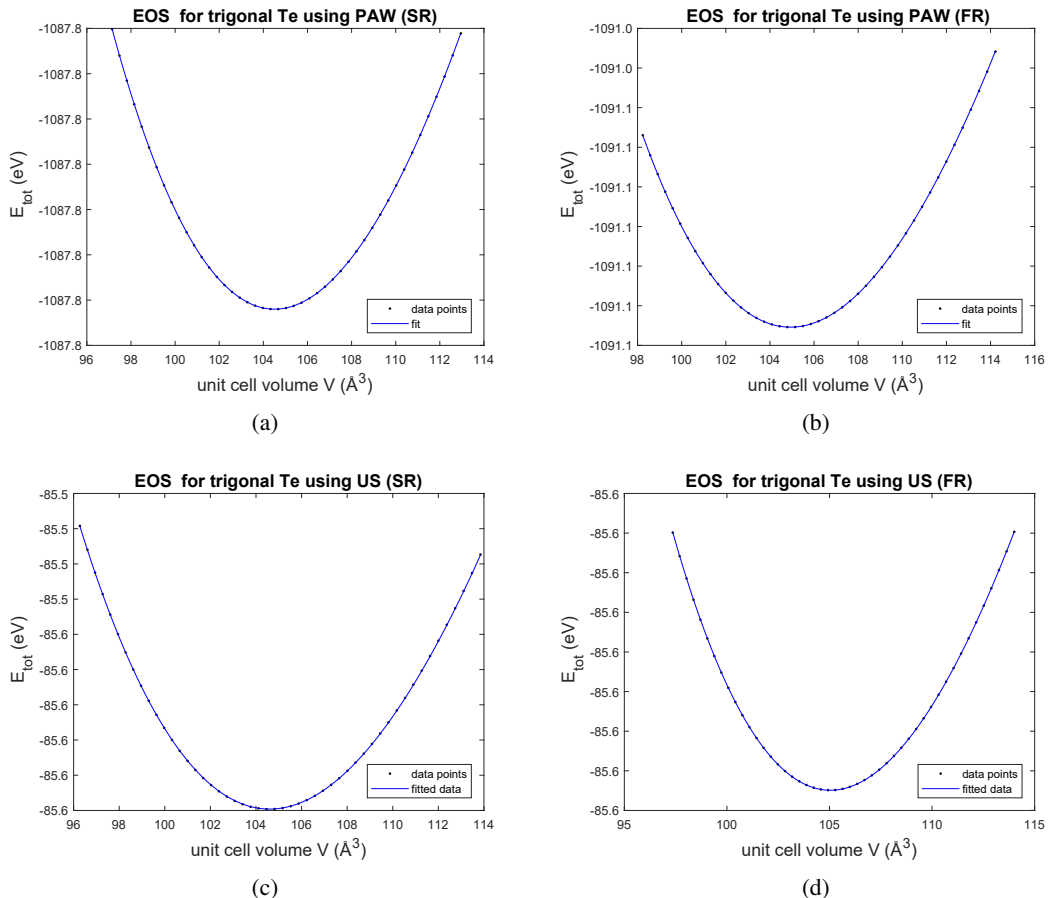


Figure 3.25. Calculated data points and fitted curves for the EOS of trigonal Tellurium: (a) Shows the data point and fit for scalar relativistic PAW pseudopotential. (b) Shows the data point and fit for fully relativistic PAW pseudopotential. (c) Shows the data point and fit for scalar relativistic ultrasoft pseudopotential. (d) Shows the data point and fit for fully relativistic ultrasoft pseudopotential.

4. Conclusion and outlook

In this project the band structures of monolayer and fewlayer and Bulk TMDs have been studied for the case of MoS₂ and WTe₂: The calculations have been carried out using DFT as implemented in Quantum Espresso using pseudopotentials from PSlibrary. The calculated results are found to be in good agreement with experimental results and what has previously been reported. In our calculations it is shown that the proper characteristics of the band structure of monolayer MoS₂ is only recovered when using pseudopotentials including the effects of spin-orbit coupling. The calculations using pseudopotentials form PSlibrary are shown to give good results that are comparable with others used in the literature. Moving on a continued study of the pseudopotentials generated with PSlibrary would be of interest, performing calculations for more systems and comparing the computational cost for different pseudopotentials. In addition to this the pseudo potentials could be used to calculate the electronic structure of a heterojunction TMDs, comparing how the electronic structure is modified by the presence of two different types of TMDs.

5. Acknowledgments

I would like to thank my supervisors Biplab Sanyal and Raquel Esteban Puyuelo for their help with this thesis. This project would not have been possible to complete without their patient help on problems along the way and their thoughtful remarks on this report.

References

- [1] K. S. Novoselov, A. K. Geim, S. V. Morozov, D. Jiang, and e. al, “Electric field effect in atomically thin carbon films,” *Science*, vol. 306, pp. 666–9, Oct 22 2004.
- [2] A. K. Geim and K. S. Novoselov, “The rise of graphene,” *Nature Materials*, vol. 6, p. 183, Mar 2007.
- [3] K. S. Novoselov, V. I. Falkó, L. Colombo, P. R. Gellert, M. G. Schwab, and K. Kim, “A roadmap for graphene,” *Nature*, vol. 490, p. 192, Oct 2012.
- [4] F. Schwierz, “Graphene transistors,” *Nature Nanotechnology*, vol. 5, p. 487, May 2010.
- [5] Q. H. Wang, K. Kalantar-Zadeh, A. Kis, J. N. Coleman, and M. S. Strano, “Electronics and optoelectronics of two-dimensional transition metal dichalcogenides,” *Nature Nanotechnology*, vol. 7, p. 699, Nov 2012.
- [6] B. Radisavljevic, A. Radenovic, J. Brivio, V. Giacometti, and A. Kis, “Single-layer MoS₂ transistors,” *Nature Nanotechnology*, vol. 6, p. 147, Jan 2011.
- [7] N. W. Ashcroft and N. D. Mermin , *Solid state physics*. 10 Davis Drive Belmont, CA 94002-3098, USA: Brooks/Cole, 1976.
- [8] Original PNGs by DrBob, traced in Inkscape by User:Stannered.
https://commons.wikimedia.org/wiki/File:Sketch_Pseudopotentials.png#/media/File:Sketch_Pseudopotentials.png. Accessed: 2018-05-14 [GFDL (<http://www.gnu.org/copyleft/fdl.html>) or CC-BY-SA-3.0 (<http://creativecommons.org/licenses/by-sa/3.0/>)].
- [9] Bilbao crystallographic server. <http://www.cryst.ehu.es/>. Accessed: 2018-05-08.
- [10] P. Strange, *Relativistic Quantum Mechanics: With Applications in Condensed Matter and Atomic Physics*. Cambridge University Press, 1998.
- [11] G. Dresselhaus, “Spin-orbit coupling effects in zinc blende structures,” *Phys. Rev.*, vol. 100, pp. 580–586, Oct 1955.
- [12] R. M. Martin, *Electronic structure : basic theory and practical methods*. The Edinburgh Building, Cambridge CB2 2RU, UK: Cambridge University press, 2008.
- [13] W. Kohn, “Nobel lecture: Electronic structure of matter—wave functions and density functionals,” *Rev. Mod. Phys.*, vol. 71, pp. 1253–1266, Oct 1999.
- [14] K. Burke, “Perspective on density functional theory,” *The Journal of Chemical Physics*, vol. 136, no. 15, p. 150901, 2012.
- [15] D. J. Singh and L. Nordström, *Planewaves, Pseudopotentials and the LAPW Method*. Boston, MA: Springer US, 2006.
- [16] M. C. Payne, M. P. Teter, D. C. Allan, T. A. Arias, and J. D. Joannopoulos, “Iterative minimization techniques for ab initio total-energy calculations: molecular dynamics and conjugate gradients,” *Rev. Mod. Phys.*, vol. 64, pp. 1045–1097, Oct 1992.

- [17] W. Kohn and L. J. Sham, “Self-consistent equations including exchange and correlation effects,” *Phys. Rev.*, vol. 140, pp. A1133–A1138, Nov 1965.
- [18] J. P. Perdew and K. Burke, “Comparison shopping for a gradient-corrected density functional,” *International Journal of Quantum Chemistry*, vol. 57, no. 3, pp. 309–319, 1996.
- [19] W. Quester. https://commons.wikimedia.org/wiki/File:Sketch_Pseudopotentials.png#/media/File:Sketch_Pseudopotentials.png. Accessed: 2018-04-25.
- [20] P. E. Blöchl, “Projector augmented-wave method,” *Phys. Rev. B*, vol. 50, pp. 17953–17979, Dec 1994.
- [21] D. Vanderbilt, “Soft self-consistent pseudopotentials in a generalized eigenvalue formalism,” *Phys. Rev. B*, vol. 41, pp. 7892–7895, Apr 1990.
- [22] A. D. Corso, “Pseudopotentials periodic table: From H to Pu,” *Computational Materials Science*, vol. 95, pp. 337 – 350, 2014.
- [23] P. Giannozzi *et al.*, “Advanced capabilities for materials modelling with Quantum Espresso,” *Journal of Physics: Condensed Matter*, vol. 29, no. 46, p. 465901, 2017.
- [24] K. Momma and F. Izumi, “VESTA3 for three-dimensional visualization of crystal, volumetric and morphology data,” *Journal of Applied Crystallography*, vol. 44, pp. 1272–1276, Dec 2011.
- [25] Z. Liu, L. Ma, G. Shi, W. Zhou, Y. Gong, S. Lei, X. Yang, J. Zhang, J. Yu, K. P. Hackenberg, A. Babakhani, J.-C. Idrobo, R. Vajtai, J. Lou, and P. M. Ajayan, “In-plane heterostructures of graphene and hexagonal boron nitride with controlled domain sizes,” *Nature Nanotechnology*, vol. 8, p. 119, Jan 2013.
- [26] B. E. Brown, “The crystal structures of WTe₂ and high-temperature MoTe₂,” *Acta Crystallographicica*, vol. 20, pp. 268–274, Feb 1966.
- [27] X. Qian, J. Liu, L. Fu, and J. Li, “Quantum spin hall effect in two-dimensional transition metal dichalcogenides,” *Science*, vol. 346, no. 6215, pp. 1344–1347, 2014.
- [28] P. A. Young, “Lattice parameter measurements on molybdenum disulphide,” *Journal of Physics D: Applied Physics*, vol. 1, no. 7, p. 936, 1968.
- [29] K. F. Mak, C. Lee, J. Hone, J. Shan, and T. F. Heinz, “Atomically thin mos₂: A new direct-gap semiconductor,” *Phys. Rev. Lett.*, vol. 105, p. 136805, Sep 2010.
- [30] K. K. Kam and B. A. Parkinson, “Detailed photocurrent spectroscopy of the semiconducting group VIB transition metal dichalcogenides,” *The Journal of Physical Chemistry*, vol. 86, pp. 463–467, Feb 1982.
- [31] X. Fan, D. J. Singh, and W. Zheng, “Valence Band Splitting on Multilayer MoS₂: Mixing of Spin-Orbit Coupling and Interlayer Coupling,” *The Journal of Physical Chemistry Letters*, vol. 7, pp. 2175–2181, jun 2016.
- [32] L. Sun, J. Yan, D. Zhan, L. Liu, H. Hu, H. Li, B. K. Tay, J.-L. Kuo, C.-C. Huang, D. W. Hewak, P. S. Lee, and Z. X. Shen, “Spin-orbit splitting in single-layer mos₂ revealed by triply resonant raman scattering,” *Phys. Rev. Lett.*, vol. 111, p. 126801, Sep 2013.
- [33] F. Birch, “Finite elastic strain of cubic crystals,” *Phys. Rev.*, vol. 71, pp. 809–824, Jun 1947.
- [34] e. John R. Rumble, *Pseudopotentials*. CRC Press/Taylor Francis, Boca Raton, FL., 2018.

- [35] F. H. Featherston and J. R. Neighbours, “Elastic constants of tantalum, tungsten, and molybdenum,” *Phys. Rev.*, vol. 130, pp. 1324–1333, May 1963.
- [36] P. Ghosh, M. U. Kahaly, and U. V. Waghmare, “Atomic and electronic structures, elastic properties, and optical conductivity of bulk te and te nanowires: A first-principles study,” *Phys. Rev. B*, vol. 75, p. 245437, Jun 2007.
- [37] G. Parthasarathy and W. B. Holzapfel, “High-pressure structural phase transitions in tellurium,” *Phys. Rev. B*, vol. 37, pp. 8499–8501, May 1988.